Broad spectrum photocatalytic system based on BiVO$_4$ and NaYbF$_4$:Tm^{3+} upconversion particles for environmental remediation under UV-vis-NIR illumination

S. Ullah[a,b], E.P. Ferreira-Neto[a], C. Hazra[a,*], R. Parveen[c], H.D. Rojas-Mantilla[a], M.L. Calegaro[c], Y.E. Serge-Correales[a], U.P. Rodrigues-Filho[c], S.J.L. Ribeiro[a,*]

[a] Institute of Chemistry, São Paulo State University (UNESP), PO Box 355, Araraquara, 14801-970, SP, Brazil
[b] Institute of Chemical Sciences, University of Peshawar, PO Box 25120, Peshawar, Pakistan
[c] Institute of Chemistry of São Carlos, University of São Paulo, 13560-970, São Carlos, SP, Brazil

A B S T R A C T

The development of photocatalysts responsive towards a broader region of the solar (UV-to-NIR) light is important for efficient harvesting of sunlight for photochemical and photoelectrical applications. In this study, two photocatalytic systems (BV/LEDs and BV/UCPs where UCPs stands for NaYbF$_4$:Tm^{3+} upconversion particles) based on bismuth vanadate (BV) are introduced for photocatalytic degradation of both organic dyes (crystal violet, CV) and pharmaceuticals (sulfathiazole, STZ) under a variety of photoactivation modes including low-power (1.26 W) LEDs and near infrared (NIR) irradiation as well as natural sunlight. The BV/LEDs system makes use of the perfect match between the emission profile of commercial blue LEDs (460 ± 10 nm) and absorption profile of BV (E$_g$ = 2.6 eV) to effectively photodegrade pollutants. The BV/UCPs system, on the other hand, exploits the NIR-to-UV/visible upconverted light from UCPs to allow photodegradation of pollutants under NIR illumination. Moreover, we present a detailed study of the experimental parameters to obtain BV particles with tailored morphology (spherical, rod-like, hyperbranched), crystalline phase (monoclinic, tetragonal or heterojunction biphasic BV) and band gap energy (2.4–2.9 eV). Depending on the phase composition, a synergetic effect in photoactivity is observed in samples containing around 68% monoclinic and 30% tetragonal BV which is ascribed to the formation of monoclinic/tetragonal heterojunction.

1. Introduction

During the last couple of centuries, anthropogenic activities have adversely affected our biosphere giving rise to the challenging problems of environmental pollution and enervation of available energy resources. According to the 2017 WHO report, around 844 million people still lack access to clean drinking water [1]. The situation becomes worst in case of natural disasters such as floods and earthquakes. Thus, there is a need to develop effective strategies for addressing these serious issues of pollution and exhaustion of available energy and natural resources.

Various strategies for pollution control and water purification have been developed including chemical oxidation, biological treatment, activated carbon adsorption, flocculation, filtration, sterilization by chlorination and the recently-developed advanced oxidation methods (AOMs), each method carrying its own advantages and disadvantages.

The AOMs, which include photocatalysis, electrochemical, photo-electrochemical, UV/ozonation, Fenton and photo-Fenton processes, employ catalytic and photochemical reactions to oxidize organic matter present in water bodies, air and soil [2–5]. Heterogeneous photocatalysis [6–9] based on semiconductors (TiO$_2$, ZnO, WO$_3$, BiVO$_4$, CdS) is one of the mostly widely studied AOMs as it leads to a more complete mineralization of the pollutants molecules.

However, the most efficient and widely used photocatalysts (TiO$_2$ and ZnO, for instance) have wider band gaps (3.2 eV for TiO$_2$) [6,10] and require UV light for photoexcitation of their valence band electrons to conduction band. Thus the requirement of continuous supply of UV light [9,11–14], which constitutes only a minor fraction (< 6%) of the solar spectrum, is the most relevant practical limitation of these important wide-band gap photocatalysts. There is, thus, a surge in research interest directed towards the synthesis of new and efficient photocatalytic materials [15–25] able to utilize a wider portion of solar

spectrum [7,15,26–36]. Moreover, the design of new light sources and the reactor-related aspects (mass transport, reactive surface and light field in the reactor) are important for the development of better photocatalytic reactors/systems. Since solar energy is considered an abundant, inexhaustible and promising source of energy, it can be usefully utilized for photochemical and photoelectric applications such as pollution control and energy production using semiconductors. The development of new photocatalytic materials responsive to a wider range of the solar spectrum (UV-to-NIR) is of great importance for effective utilization of solar energy for both photochemical and photoelectrical applications.

Among the visible-light responsive photocatalysts, monoclinic bismuth vanadate (BV) has recently emerged as one of the most promising non-titania photocatalysts for photocatalytic applications, especially pollutants photodegradation [36–40] and water oxidation [41–44], under visible light irradiation. Moreover, the ability of BV to achieve oxygen evolution from water, a challenging phenomenon which is vital for complete water-splitting, has also drawn researchers' attention [41–44]. Despite its limitation such as slow kinetics for oxygen evolution and poor electron transport properties, BV is still considered one of the most important photocatalysts for water oxidation and pollutants degradation and a large body of scientific research has been directed towards improvement of its photocatalytic efficiency [41,44] through different strategies such as metal doping [45], facets and morphology tailoring [46,47] and heterojunctions formation [37,39,42,48].

Owing to its unique photocatalytic properties under visible light, different methods [39,42,45–47,49] have been developed to synthesize BV in different crystalline phases with tailored morphologies [41,44]. Among these methods, microwave-assisted hydrothermal method is regarded as a rapid and promising alternative to the conventional hydrothermal methods [50] for the synthesis of nanomaterials. Since microwaves have greater penetrability and low thermal gradient, they allow uniform and rapid heating and thus faster reaction kinetics. Moreover, microwave-assisted approaches allow more flexibility with respect to controlling the synthesis conditions (time, temperature and pressure during the hydrothermal treatment, for instance) as well as observation of the crystals as they grow [15]. These inherent advantages make the microwave-assisted synthetic strategies ideal for nanomaterials synthesis.

Though there have been many efforts directed towards the extension of semiconductor photocatalysis towards visible region, the development of photocatalytic systems responsive towards NIR region is relatively less reported. One way to develop NIR-active photocatalytic system is to combine semiconductors photocatalysts (TiO$_2$ or ZnO, for instance) with upconversion particles (UCPs) based on rare-earth fluorides/oxides such as NaYF$_4$: Yb^{3+}/Tm^{3+} [15,28,31,32]. Upconversion (UC) is a nonlinear optical process whereby successive absorption of two or more source photons (usually from a laser), *via* intermediate long-lived energy states, is followed by the emission of the output photons with shorter wavelength than the incident photons [51,52]. The upconverted light emitted by the UCPs in the visible and UV region upon NIR excitation can be utilized to excite the semiconductors photocatalyst [15]. Though there are quite a few reports on the preparation of UCPs-TiO$_2$/ZnO systems [15,28–35,53], these wideband semiconductors absorb only the UV portion of the NIR-to-UV/Visible upconverted light from UCPs. Since most of the UCPs exhibit stronger visible than UV emission, in this study, we have chosen BV/UCPs photocatalytic system where the narrow band-gap (E$_g$ = 2.6 eV) of BV allows to harvest a major portion of the NIR-to-UV/visible upconversion emission from UCPs, in addition to the visible portion of natural sunlight, thus making the system responsive to a wider range (UV-to-NIR) of the electromagnetic spectrum.

Furthermore, most of the reports in literature on photocatalytic applications of semiconductors are based on the use of mercury or xenon lamps as illumination sources. Recently, UV light-emitting diodes (LEDs) light sources have attracted attention for use in photocatalysis

[54–59] as they offer advantages of longer life time (50,000 h), low cost, high reliability, small size, light weight, environmental safety, higher current-to-light conversion efficiency (40%) and lower operational temperature (∼ 40 °C) and voltage (1.5–5 V) [56,60]. One of the prominent advantages of using LEDs is their operation using DC power supply, which allows application of LEDs-based photocatalysis in remote and isolated areas.

From an environmental point of view, the extensive use of organic dyes, especially in the textile industry [61], and pharmaceuticals has become a major environmental concern as these pollutants lead to lasting effects on ecosystem and human health [62–64]. For instance, around 50–90% of ingested pharmaceutical drugs are excreted in unmetabolized form causing soil and water pollution. Sulfathiazole (STZ) is an antimicrobial drug widely used in veterinary industry and is considered one of the emerging micropollutants [63,64]. The presence of STZ in aquatic environment has been associated with several problems such as decreased growth rate of freshwater vertebrates and changes in the steroidogenic pathway, sexual hormones balance and reproductive endpoints (time to hatch and growth) in fishes [63,64]. To address these serious environmental problems related to the indiscriminate use of antibiotics and large-scale production/usage of synthetic organic dyes, there is a need to develop innovative and environmentally friendly treatment technologies.

Thus, in this study, we have successfully prepared Tm^{3+}-doped NaYbF$_4$ UCPs and highly crystalline BV in pure monoclinic phase or mixed monoclinic/tetragonal phases using a simple and facile microwaves-based hydrothermal method which requires a short reaction time for obtaining samples with good crystallinity. Moreover, we have employed very low-power (1.26 W) 460 nm blue LEDs as the light source for photoactivation of BV and still achieved good photocatalytic activity, as measured by the photodegradation of CV dye and veterinary pharmaceutical STZ. Such high visible light photoactivity of the prepared samples is attributed to the good crystallinity of BV as well as a close match between the emission profile of the LEDs and the absorption profile of monoclinic BV, thus allowing efficient photodegradation of organic molecules. Moreover, the prepared BV particles were found to exhibit excellent photoactivity towards organic molecules (CV dye, and STZ) under natural sunlight illumination. Finally, we have demonstrated that the NIR-to-UV/visible upconverted light from NaYbF$_4$:Tm^{3+} UCPs could be used to photoexcite BV and, resultantly, photodegrade organic dyes. While the visible-light activity of BV may allow effective harvesting of the solar energy for photoelectrochemical applications during daylight, the low-cost LED-based illumination system/reactor is promising for photocatalytic remediation of pollutants in remote and isolated areas using low-power DC power supply, even in the night time.

2. Experimental

2.1. Synthesis of bismuth vanadate (BiVO$_4$)

Bismuth vanadate, predominantly in monoclinic scheelite phase, was prepared by a rapid microwave-assisted hydrothermal method using a commercial microwave synthesizer system (Model Discover SP-909150, CEM Corp., USA). Briefly, 10 mmol of NH$_4$VO$_3$ (99% Sigma-Aldrich) were dissolved in hot water (90 °C) and finally diluted to 150 mL with deionized water (18.2 MΩcm). Similarly, a stock solution (10 mmol, 0.1 L) of Bi(NO$_3$)$_3$·5H$_2$O (Sigma-Aldrich) was prepared by dissolving Bi(NO$_3$)$_3$·5H$_2$O in 1 M HNO$_3$ (Qhemis, Brazil) solution. Then 15 mL (1 mmol) of the NH$_4$VO$_3$ stock solution were dropwise added to 10 mL (1 mmol) of Bi(NO$_3$)$_3$ solution in a glass beaker and the resulting orange yellow solution had a pH around 1. After adjusting the pH (1–9.5 pH) of the sample suspension with NH$_4$OH (25%, Qhemis, Brazil), the mixture was transferred to a 35-mL glass pressure vessel (CEM Part no. 909036) and exposed to microwave irradiation at a microwave power of 200 W for different intervals of times (5–60 min)

and different reaction temperatures (120–190 °C) under constant magnetic stirring. After this microwave-assisted hydrothermal treatment, the resulting BV suspension was centrifuged at 6000 rpm, washed once with ethanol and twice with deionized water and finally dried at 60 °C for 24 h. The sample codes BV(pH1) and BV(10 min) used in the text denote the BV samples prepared at pH 1 (at fixed microwave time of 15 min) and microwave treatment time of 10 min (at fixed pH = 6), respectively.

2.2. Synthesis of NaYb₄:Tm³⁺ (0.5%) upconversion particles (UCPs)

The hexagonal $NaYbF_4$ upconversion microrods doped with Tm^{3+} were prepared by a facile co-precipitation/MW-assisted hydrothermal method according to our previous report [15]. In a typical synthesis, 2.07 mL $Yb(NO_3)_3$ solution (0.48 mol L^{-1}) and 0.5 mL of $Tm(NO_3)_3$ solution (1.0×10^{-2} mol L^{-1}) were added to 10 mL of EDTA solution (0.2 mol L^{-1}) and kept under magnetic stirring for 30 min. Upon addition of 15 mL NaF solution (1 mol L^{-1}), co-precipitation led to the formation of a colloidal suspension which was subjected to microwave-assisted hydrothermal treatment for 1 h at 180 °C, pressure of 17.2 bars and microwave power of 200 W. The obtained UCPs were centrifuged at 8000 rpm, washed once with ethanol and twice with deionized water using centrifugation/re-suspension cycles and finally dried at room temperature. To remove the EDTA from their surface, the UCPs were heated at 400 °C for 90 min.

2.3. Photocatalytic activity measurement

In order to compare the photocatalytic response of different BV samples, their photocatalytic activity was evaluated through photodegradation of CV dye (10 mg L^{-1}) under controlled visible light illumination provided by the blue-emitting (460 ± 10 nm) LEDs and UV–vis light from a xenon-mercury lamp (Lightningcure LC8, Hamamatsu, Japan) with a light intensity output of 9.7 and 18.5 mW/cm² at 460 nm and 365 nm, respectively. For measurement of visible light activity, 21 LEDs (total electric power = 1.26 W, light intensity output at 460 nm = 2.5 mW/cm²), arranged in three rows and powered by a 25 V power source, were attached to the Teflon-made lid of a cylindrical glass reactor (diameter 10.5 cm, height 5.5 cm) so that the reaction mixture inside the reactor could be uniformly illuminated from the top. Typically, 50 mg of BV sample was suspended in 25 mL of water and dispersed through sonication. The BV aqueous suspension was then added to 25 mL of CV solution and the mixture (50 mL) was left to stir for 1 h in dark. Subsequently, the BV/CV mixture was exposed to visible light irradiation from the LEDs source (or UV–vis light from Xe-Hg lamp) for different intervals of time and the temporal changes in absorption of CV were monitored by taking the electronic absorption spectra of the supernatant part obtained after centrifugation using Cary 5000 UV–vis-NIR spectrophotometer. In the Recycling experiments carried out in identical fashion, the used photocatalyst was recovered by centrifugation and added to a fresh batch of CV solution for the next photocatalytic cycle. The photocatalytic activity measurements under natural solar light irradiation were performed under identical conditions except that a borosilicate tube (diameter, length) containing the CV/BV mixture was used as reactor and exposed to natural sunlight (location: Araraquara, SP, Brazil, −21.806806 (latitude), −48.192575 (longitude); time: 11 h–13 h; average daily horizontal irradiance: 4.72 kW h/m²/day (April)).

Similar procedure was applied for the photocatalytic degradation of sulfathiazole (STZ) (0.5 g L^{-1} of BV, 100 mL reaction volume, 150 μg L^{-1} STZ). The concentration of STZ as function of blue-LEDs illumination or natural sunlight illumination was monitored by measurement of the HPLC chromatograms of the filtered (0.45 μm syringe filter) sample aliquots using an LC-20AT chromatograph (Shimadzu) equipped with a diode array detector (DAD SPD-M20A) and C-18 column (250 mm × 4.6 mm) under fixed chromatographic conditions

(mobile phase: methanol/0.1% acetic acid mixture (15/85%), flow rate: 1 mL min⁻¹, injection volume: 50 μL, temperature: 40 °C and detector measurement wavelength = 284 nm, detection limit: 5 μg L^{-1}, quantification limit: 16 μg L^{-1}).

To test the photocatalytic activity of $NaYbF_4$:Tm^{3+}/BV system and $NaYbF_4$:Tm^{3+}/TiO_2 system under NIR irradiation, 5 mg of the UCPs and 5 mg of BV (or P25 TiO_2) were suspended in 1.5 mL of deionized water and dispersed by sonication for 30 min. Then 1.5 mL aqueous solution of CV (10 mg L^{-1}) was mixed with it and the dye/photocatalyst mixture (3 mL) left in dark for 12 h to attain adsorption/desorption equilibrium. The dye/UCPs/BV mixture in a quartz cuvette was irradiated with a 980 nm NIR laser at a power of 1 W using an optical fiber of 200 μm diameter. After each 1 h of NIR illumination, a 1 mL aliquot was centrifuged at 7000 rpm for 3 min and the UV–visible absorption spectra of the supernatant was measured using a spectrophotometer. The sample aliquot was transferred back to the reaction mixture after taking its electronic spectrum. Similar procedure was used for photodegradation of STZ under NIR (980 nm) illumination. In this case, 2 mL of 150 μg L^{-1} STZ was added to 1.5 mL suspension containing 5 mg of UCPs and BV each. To confirm the photoexcitation of BV through the upconverted light upon 980 nm excitation of the $NaYbF_4$:Tm^{3+}, the formation of ˙OH radicals formed in the irradiated terephthalic acid/UCPs/BV mixture was monitored by measurement of the fluorescence spectra of terephthalic acid ($\lambda_{(ex)}$ = 315 nm, $\lambda_{(em)}$ = 425 nm) before and after NIR irradiation [66].Terephthalic acid solution (4×10^{-4} mol L^{-1}) was prepared by dissolving its calculated amount in aqueous NaOH solution (2×10^{-3} mol L^{-1}) [66]. To compare the photoactivity of different samples and calculate the observed rate constant (k_{obs}), the kinetic profiles ($\frac{C}{C_0}$ vs. time) for different samples were fitted using a first order exponential function using the equation, $\frac{C}{C_0} = e^{-k_{obs} \cdot t}$.

2.4. Characterization techniques

The scanning electron microscopy (SEM) micrographs of BV samples deposited as thin layer on single crystal silicon substrates were acquired using a LEO 440 (UK) microscope. Powder X-ray diffractograms of the BV samples were acquired with a D8 Advance X-ray diffractometer (Bruker) operated at operated at 40 mA and 40 kV employing Ni-filtered Cu Kα X-ray radiation (λ = 1.540 Å). The XRD structures were refined by the Rietveld method [67] using the DIFFRAC TOPAS v5 software solution from Bruker. The diffuse reflectance (DR) spectra of the powder samples were obtained with a Cary 5000 UV–vis-NIR spectrophotometer (Varian) against a background of $BaSO_4$ and were transformed into Kubelka-Munk (K-M) function, $F(R_\infty) = \frac{(1 - R_\infty)^2}{2R_\infty}$, where $F(R_\infty)$ is the remission or Kubelka-Munk function and R_∞ is the ratio between the reflectance of the sample and the reference ($BaSO_4$, here) [68,69]. The Band gap energy (E_g) was obtained by extrapolating the linear portion of the plot between $[F(R_\infty) h\nu]^2$ against $h\nu$ to y-axis = 0. Raman spectra of the samples were collected with a LabRAM HR 800 model Raman Spectrophotometer (Horiba Jobin Yvon) equipped with CCD detector (model DU420A-OE-325) and a He–Ne laser (632.81 nm). The spectra were taken between 100 and 1000 cm⁻¹ with acquisition time of 50 s and 2 cycles. The photoluminescence emission spectra of $NaYbF_4$:Tm^{3+} and $BiVO_4$ ($\lambda_{(exc)}$ = 375 nm) powders were acquired using a Horiba Jobin Yvon spectrofluorometer (model fluorolog-3 FL3-122). A 980 nm laser diode (0.5 W power) coupled with an optical fiber (200 μm diameter) was utilized as the excitation source for UCPs. To evaluate the mineralization efficiency of BV during CV photodegradation, measurement of total organic carbon (TOC) was carried using a Shimadzu TOC-V$_{CPN}$ analyzer.
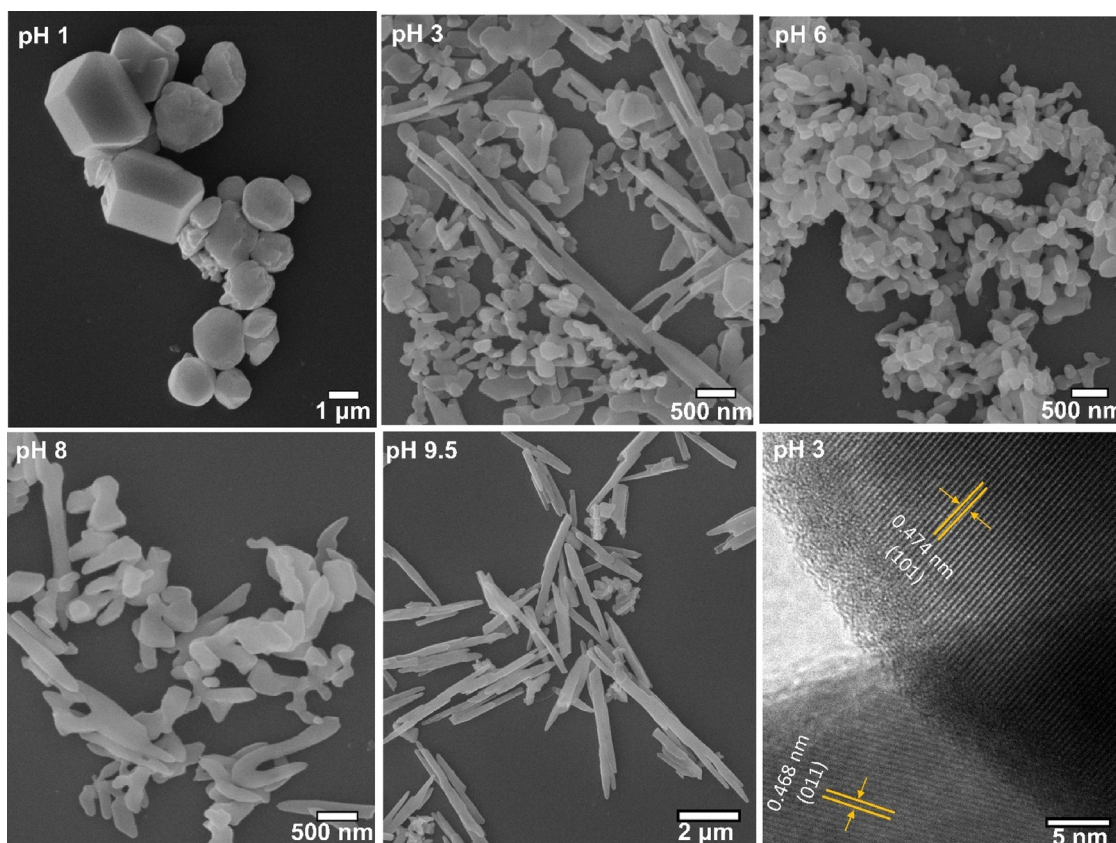
Fig. 1. SEM images of BV samples prepared using different pH during the synthesis at constant microwave treatment time (15 min) and temperature (180 °C). The representative HRTEM image of BV(pH3) sample is also shown in the lower right-hand side corner of the Figure.

3. Results and discussion

3.1. Morphological and physicochemical characterization of bismuth vanadate

The SEM images in Fig. 1 exhibit the evolution of BV particle morphology/size as function of pH of the reaction media. Apparently, pH of the solution seems to strongly affect the morphology, surface textures and shape of the BV samples. Except at pH 1, the prepared BV samples consist of hyperbranched micro/nanocrystals. Large irregular and aggregated particles (2 ± 0.5 μm) are formed in the as-prepared samples with no pH adjustment (pH ~1). The samples prepared at pH 3, 6 and 8 have at least one dimension in nanometric range. The sample prepared at pH 3 consists of a mixture of small spheroidal particles and sheet or plate-like particles. At higher pH (pH~9), the branched particles tend to partially convert into microrods. It has been proposed that pH affects the concentration of free Bi^{3+} ions in solution and thus the rate of nucleation/growth processes, leading to slower kinetics at such higher pH which favour anisotropic growth of the particles [70]. The HRTEM image (Fig. 1) of BV(pH3) sample confirms its high crystallinity and the interplanar distance values of 0.474 and 0.468 nm observed correspond to the (101) and (011) atomic planes of monoclinic BV (PDF no. 75–2480).

Fig. S1 shows the effect of microwave-assisted hydrothermal treatment time on the morphology of the prepared BV samples. It can be noted that larger aggregated particles with no definite morphology are formed in sample prepared without microwave treatment. Upon microwave exposure, however, BV particles with at least one dimension in nanometric regime and a hyperbranched morphology are obtained. Similar to microwave exposure time, the temperature during the microwave-assisted hydrothermal treatment also assists in obtaining product with definite texture and morphology (Fig. S2). While the as-prepared sample (without microwave treatment) and samples prepared at lower temperature (120 °C) consist of large irregular particles, products with smaller dimensions and a hyperbranched texture are obtained at higher temperatures (140–200 °C) (Fig. S2). These results confirm that the microwave-assisted hydrothermal treatment is effective and important for controlling the morphology as well as crystallinity of the product (*vide infra*). EDX analysis (Fig. S3) of the BV(pH3) sample shows the presence of emission peaks attributed to Bi, O and V with an estimated average atomic composition of $Bi_1V_1O_{3.6}$ and elemental composition of around 67% Bi, 15.6% V and 17.4% O.

To probe their local structure and bonding states, the BV samples prepared under different reaction conditions (pH, microwave treatment time and temperature) were characterized by Raman spectroscopy. Fig. S4a compares the Raman spectra of BV samples with and without microwave-assisted hydrothermal treatment. Except for the prominent bands at 825 cm^{-1}, assigned to the symmetric stretching modes of V−O bonds, no clearly defined Raman vibrational modes of any crystalline phase of BV are observed in the as-prepared sample without microwave treatment. However, clear and well-defined vibrational modes of monoclinic scheelite phase of BV [50,71] are seen after 5 min of microwave treatment time (Fig. S4a) which reveals the importance of microwave treatment for obtaining crystalline BV sample with well-defined structures and symmetries.

As shown in Fig. 2a, Raman spectra of BV samples prepared using different MW treatment times at fixed pH and fixed temperature are almost similar in shape and form and exhibit vibrational bands at 124, 212, 327, 367, 712 and 825 cm^{-1} which can be ascribed to the monoclinic scheelite type BV [50,71]. The Raman bands at 124 and 212 cm^{-1} arise from external modes (translation/rotation), those at 327 cm^{-1} and 367 cm^{-1} correspond to the antisymmetric and symmetric bending modes of V−O bond in the VO_4 units, respectively [50]. While the other Raman bands give little structural information, the
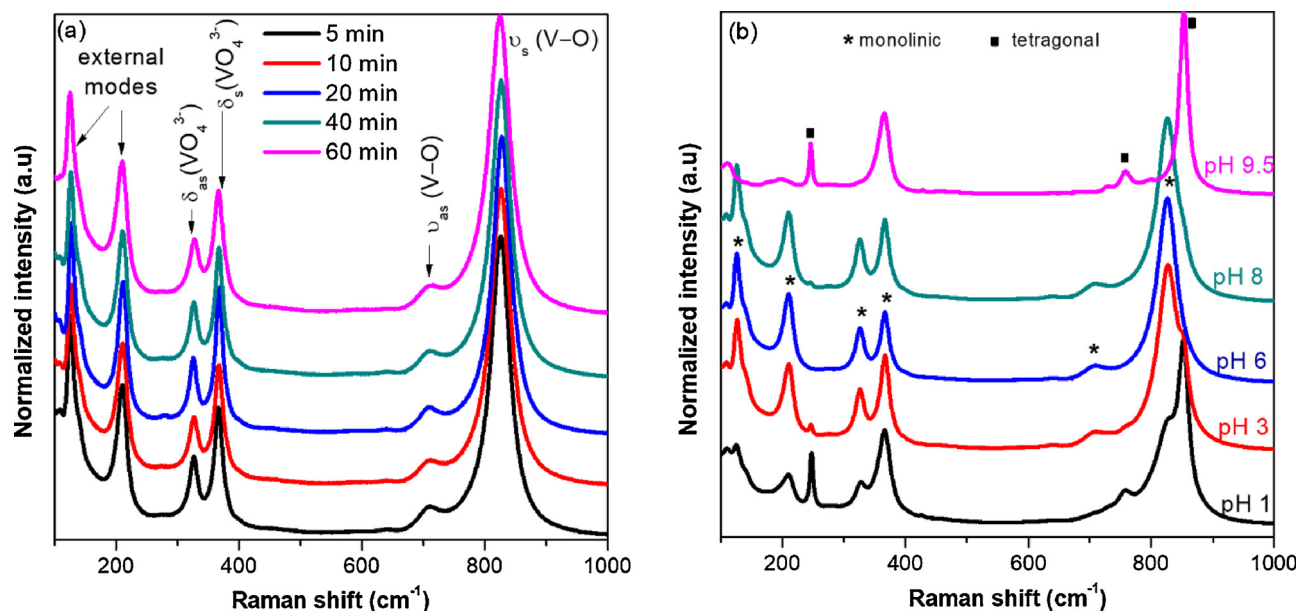
Fig. 2. Raman spectra of BV samples prepared using (a) different microwave treatment times while keeping pH (pH 6) and temperature (180 °C) fixed and (b) using different pH at a fixed microwave treatment time (15 min) and fixed temperature (180 °C). The Raman bands of monoclinic and tetragonal BV in **b** are marked with asterisk (*) and square (■), respectively.

bands at 712 and 825 cm^{-1}, respectively assigned to the antisymmetric and symmetric stretching modes of V−O bonds, are sensitive to local structural variation [50]. Since no obvious change in the position, width or intensity of these bands is observed, we infer that the BV samples prepared using different microwave exposure time have almost similar local structure. However, after a careful examination of the 730–900 cm^{-1} region (Fig. S5), some minor changes in position of the vibrational mode centered at 825 cm^{-1} (v_s(V−O)) can be observed, indicating that the local structure, though similar, is not essentially identical among the samples prepared using different microwave treatment times. Similarly, all the BV samples prepared using different microwave temperatures exhibit Raman bands characteristics of only monoclinic scheelite phase (Fig. S6).

The BV samples prepared using different solution pH show different vibrational features. As shown in Fig. 2b, the samples prepared at pH 6 and pH 8 exhibit the characteristic vibrational bands of monoclinic scheelite type BV at 124, 212, 327, 367, 712 and 825 cm^{-1} [50,71], in agreement with the XRD results (*vide infra*). The sample prepared at pH 9.5 exhibits Raman vibrational modes predominantly of tetragonal phase at 853 cm^{-1} and 754 cm^{-1} which can be assigned to the symmetric and antisymmetric V−O stretching modes of tetragonal phase of BV [71–73], respectively. The bands at 127 cm^{-1}, 212 cm^{-1} and 327 cm^{-1} are almost absent for this sample. By observing the spectral evolution, especially the vibrational bands at around 800 cm^{-1}, as function of pH, it can be observed that the BV(pH1) sample has more tetragonal phase than monoclinic one as indicated by the higher intensity of 853 cm^{-1} band compared to 825 cm^{-1} band. As the pH is increased to 3, the 825 cm^{-1} band becomes more prominent in comparison to the 853 cm^{-1} band indicating the formation of monoclinic BV as predominant phase. Further increase in pH (pH = 6) leads to the disappearance of the 853 cm^{-1} band and the formation of pure monoclinic BV. At pH > 8, the tetragonal phase becomes the predominant phase. Thus, mostly tetragonal phase is formed under highly acidic (pH < 3) or highly basic (pH > 8) conditions, monoclinic scheelite type BV is obtained under intermediate pH conditions. Moreover, the relative intensities of the asymmetric (327 cm^{-1}) and symmetric (367 cm^{-1}) bending modes of V−O bond in the VO$_4$ units are different for samples prepared at different pH which might be related to difference in phase compositions. The pH of solution thus plays a vital role in determining

not only the morphology and size of the BV samples but also the phase and local structure of the product.

The crystalline structure and phase composition of the BV samples was further analyzed by powder XRD (Fig. 3). Rietveld analysis of the diffraction data was performed in order to find out the phase composition of the prepared samples (Table 1). Fig. 3c and d are typical examples of Rietveld refined powder XRD data. The R-values included in Table S1 for each refinement performed indicate an excellent quality of fitting. No clear diffraction peaks could be observed for the sample prepared without microwave irradiation (Fig. S4b) indicating the amorphous nature of the sample. After microwave-assisted hydrothermal treatment, all samples exhibit sharp and well-defined diffraction peaks confirming that microwave treatment for as short as 5 min is sufficient to obtain BV particles with good crystallinity (Fig. S4b). The XRD patterns of all BV samples prepared using different MW treatment times (Fig. 3a) closely and predominantly match with the standard diffraction patterns of monoclinic scheelite BV (ICDD PDF no. 75-2480 and 14-0688). Nevertheless, some low intensity diffraction peaks at 2-theta values of 24.3, 32.4 and 48.4° corresponding to tetragonal zircon structure of BV (ICDD PDF no. 14-133) appear for microwave treatment time of 20 min or longer, indicating the presence of tetragonal phase as a minor (< 5%) phase, as confirmed by Rietveld analysis of the respective diffraction data (see Table 1). A fraction of Bi$_2$O$_3$ was also found to be present as a minor (< 5%) impurity in some of the samples.

The pH of the reaction, on the other hand, has a profound effect on the phase composition of BV samples (Fig. S7). As shown in Fig. 3b, the BV samples prepared at pH 1,3, 8 and 9.5 consist of a mixture of tetragonal and monoclinic BV while BV(pH6) consists of only monoclinic BV. BV(pH 3) sample contains around 68% tetragonal and 30% monoclinic phase. The proportion of monoclinic phase increases with increase in pH until pH 6 (98% monoclinic, 0% tetragonal and 2% Bi$_2$O$_3$) and, above pH 8, the tetragonal phase reappears, reaching a maximum of 90.5% at pH 9.5 (Table 1). As discussed later, the phase composition plays an important role in the photocatalytic properties of BV both under visible and UV–vis illumination.

The photophysical properties and electronic states of BV samples were studied using diffuse reflectance spectroscopy (DRS). All the BV samples prepared using different microwave treatment times show absorption in the visible region (below 530 nm) which is characteristic
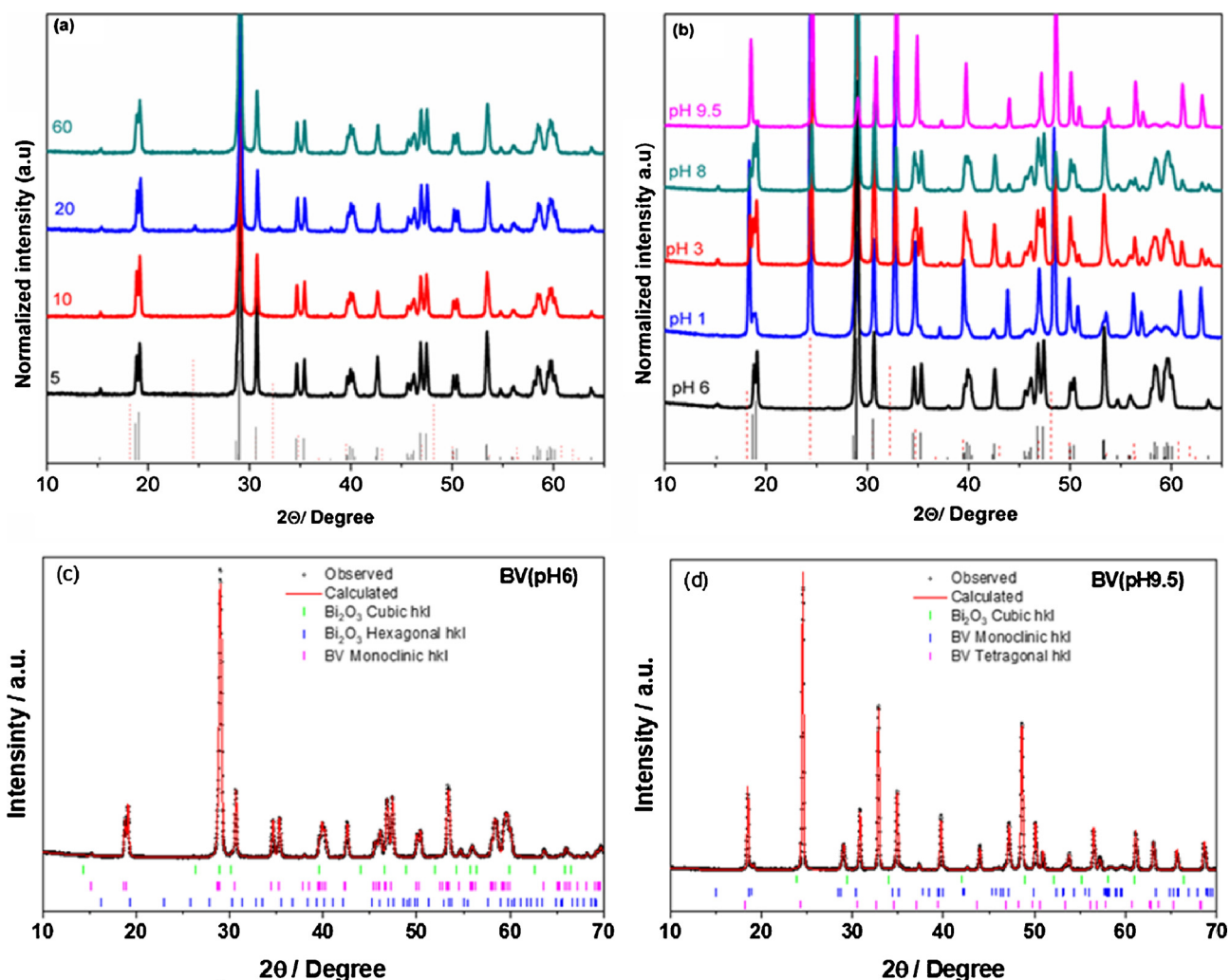
Fig. 3. XRD patterns of BV samples prepared using (a) different microwave treatment times, (b) different pH values while keeping all other conditions constant and (c,d) Rietveld refinement of powder XRD data for BV(pH6) and BV(pH9.5), respectively. For comparison, the standard diffraction patterns of tetragonal BV (PDF no. 14-133, red dotted lines) and monoclinic BV (PDF no. 75–2480, black solid lines) have also been inserted at the bottom of **a** and **b** (For interpretation of the references to colour in this figure legend, the reader is referred to the web version of this article).

of BV (Fig. S8a). Unlike other samples exposed to microwave-assisted hydrothermal treatment, the BV sample prepared without microwave treatment does not show the absorption characteristics typical of BV and the absorption intensity is also lower (dotted line Fig. S8a). Since the absorption onsets (Fig. S8a) and the band-gap energy (E_g) values

(2.60–2.63 eV) [74], estimated from K-M plot [68,69] (Fig. S8b, Table 1) considering a direct band gap for BV [75,76], do not differ significantly as function of microwave exposure time, we infer that this parameter affects little the electronic structure of these samples. Similarly, the temperature used during the microwave treatment also does

Table 1
Phase composition based on Rietveld analysis, band gap energies (E_g) and observed rate constants (k_{obs}, for photocatalytic degradation of CV dye under visible ad UV–vis light illumination) for BV samples prepared using different pH and different microwave treatment times.

Sample	Phase composition[a]		E_g (eV) (Direct gap)	k_{obs} (min^{-1})	
	Monoclinic (%)	Tetragonal (%)		LEDs (visible)	Xe/Hg lamp (UV–vis)
BV(pH1)	25.0	69.6	2.46, 2.86	0.002	0.007
BV(pH3)	68.2	30.5	2.54, 2.93	0.014	0.167
BV(pH6)	97.8	0.0	2.59	0.023	0.028
BV(pH8)	86.8	11.2	2.57, 2.92	0.011	0.018
BV(pH9.5)	9.40	90.5	2.53, 2.93	0.002	0.024
BV(5 min)	93.8	5.0	2.60	0.029	–
BV(10 min)	98.67	0.0	2.62	0.049	–
BV(20 min)	96.61	2.0	2.61	0.031	–
BV(40 min)	99.31	0.0	2.61	0.032	–
BV(60 min)	97.18	2.1	2.63	0.017	–

[a] Some of the samples contained Bi_2O_3 as phase impurity in varying portions (0.2–3%).
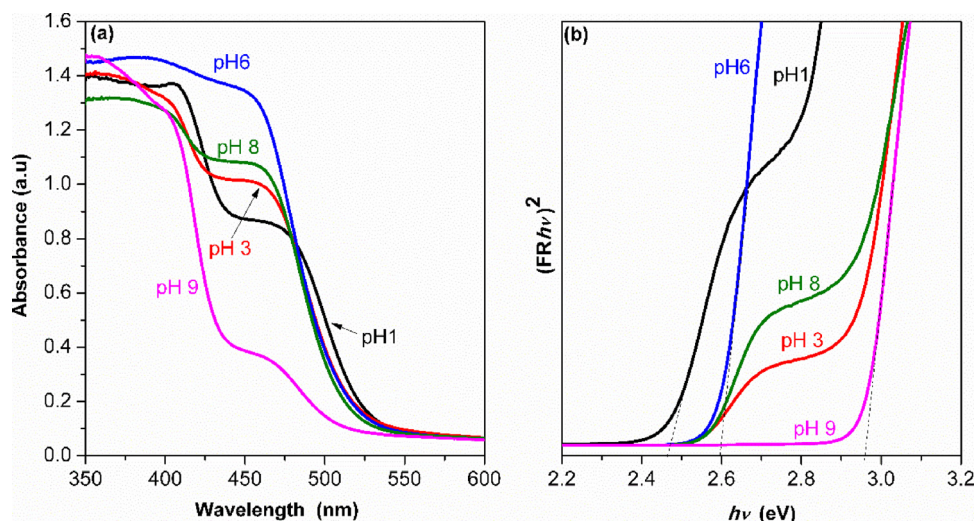
Fig. 4. (a) Absorbance spectra and (b) Kubelka-Munk transformed DRS spectra of BV samples prepared using different pH at a fixed microwave treatment time (15 min) and fixed temperatures (180 °C).

not affect the optical properties of the BV samples provided that pH of the reaction mixture is kept constant (Fig. S9).

The pH the solution used during the synthesis, on the other hand, seems to play an important role in determining the optical properties of the BV samples (Fig. 4). The phase-pure sample prepared at pH 6 consists of only monoclinic phase and thus exhibits an optical behavior typical of monoclinic BV and similar to that observed in Fig. S8a. This sample shows a single inflection point (E_g = 2.59 eV) in the K-M plot (Fig. 4b) which corresponds to the interband transition of monoclinic BV. All other samples prepared at highly acidic pH (pH 1, 3) and at highly basic pH (pH 8, 9.5) showed markedly different spectral features (Fig. 4a). For instance, the samples prepared in strongly acidic media (pH 1 and 3) show two inflection points in the K-M plot (Fig. 4b) which correspond to the band gap absorption of two different BV phases in these samples (Table 1), in accordance with the results from XRD and Raman spectroscopy. Considering the BV(pH3) sample, two different E_g values, 2.54 eV and 2.93 eV, can be calculated from the extrapolation of the linear part of the corresponding $[F(R_\infty) h\upsilon]^2$ *vs.* $h\upsilon$ curves which correspond to the monoclinic and tetragonal phases of BV [74,77], respectively.

The spectral features of BV(pH9.5) sample, which consist of around 90% tetragonal and 10% monoclinic phase, are dominated by the tetragonal phase and thus this samples shows a blue-shift and mostly absorbs in the region below 425 nm of the spectrum (Fig. 4a), despite a slight absorption in the visible region. This blue-shift in spectra of BV (pH9.5) can be ascribed to the presence of tetragonal phase of BV (see Fig. 3b, also) which exhibits higher band-gap (2.93 eV, Fig. 4b) than its monoclinic counterpart [74,77]. Compared to the E_g values of all other samples, BV(pH1) sample shows lower values for both its monoclinic (E_g = 2.46 eV) and tetragonal (2.86 eV) components. This observed red-shift in optical spectra or decrease in E_g values of BV(pH1) may be attributed to its bigger particle size (Fig. 1). As in BV(pH3) samples, the second inflection (E_g = 2.86 eV) in BV(pH1) sample corresponds to the interband transition of tetragonal BV. In the samples prepared under different pH (except BV(pH1)), the estimated average E_g values were found to be 2.55 ± 0.027 eV and 2.92 ± 0.005 eV for the monoclinic and tetragonal components of the samples, respectively. The lower values of the standard deviation show that E_g values for the same phase do not vary significantly among the samples. Among the experimental conditions used in the synthesis, pH of the reaction medium seems to strongly affect the morphology, particle size, phase composition as well as both local and electronic structure of the products.

3.2. Physical characterization and optical properties of NaYbF$_4$: Tm^{3+} UCPs

The NaYbF$_4$:Tm^{3+} UCPs were prepared by a rapid microwave-assisted hydrothermal method employing EDTA as chelating/shape-controlling agent [15]. The SEM images in Fig. 5a show that the prepared UCPs have a regular and uniform microrod morphology with an average length and diameter of 2.9 ± 0.1 μm and 0.8 ± 0.07 μm, respectively. Closer examination of the microrods reveals their hexagonal shape (inset in Fig. 5a), in accordance with the results of XRD analysis (Fig. 5c). EDX analysis of UCPs shows the emission lines characteristics of Yb, Tm, Na and F (Fig. 5b) which confirms successful incorporation of these elements in the lanthanide fluoride-based matrix of UCPs. From EDX analysis of three different samples of the same nominal composition, the average elemental composition was estimated to be 14.7% Na, 20.2% Yb, 46.5% F and 0.4% Tm which corresponds to an atomic ratio of Na$_1$Yb$_{1.3}$F$_{4.3}$:Tm$_{0.03}$.

The crystalline phase of UCPs was studied by XRD. The X-ray diffractogram of UCPs in Fig. 5c shows that NaYbF$_4$ crystallized in the thermodynamically stable hexagonal (β-NaYbF$_4$) phase (PDF 27-1427) which usually exhibits stronger UC luminescence than its more symmetrical cubic counterparts (α-NaYbF$_4$) [78,79].

Fig. 5d shows a representative UC emission spectrum of the NaYbF$_4$:Tm^{3+} UCPs under 980 nm laser excitation. The emission spectrum shows strong emission in the blue and UV region. The main emission peaks are found in the UV region at around 290, 345 and 361 nm and visible region at 450, 475 and 580 nm, all of which are characteristics of the Tm^{3+} ions [15]. The mechanism of NIR-to-UV/Vis UC in Yb^{3+}/Tm^{3+}–doped UCPs (where Yb^{3+} acts as a sensitizer and Tm^{3+} as activator) has been widely reported [80,81] and is presented in Fig. 6a. The Yb^{3+} (sensitizer) ions absorb the pump radiation (980 nm) and gets excited as a result of $^2F_{7/2} \rightarrow ^2F_{5/2}$ transition. The excited Yb^{3+} ions then transfer energy to the Tm^{3+} ions inside the NaYbF$_4$ matrix through successive energy transfer (ET) steps which results in population of the upper $^1G_4$, $^3F_2$ and $^3H_5$ levels of Tm^{3+} ions [80,81]. Population of $^1D_2$ level occurs through cross-relaxation between $^3F_2 + ^3H_4 \rightarrow ^3H_6 + ^1D_2$ [78,80,81]. Finally, as a result of another ET step, the $^1I_6$ level is populated *via* transition between $^1D_2$ and $^3P_{1,2}/^3I_6$ levels (Fig. 6a). Relaxation of the excited Tm^{3+} ions occurs with the emission of photons in the UV and visible regions of the electromagnetic spectrum at 290 nm ($^1I_6 \rightarrow ^3H_6$), 345 nm ($^1I_6 \rightarrow ^3F_4$), 361 nm ($^1D_2 \rightarrow ^3H_6$), 450 nm ($^1D_2 \rightarrow ^3F_4$) and 475 nm ($^1G_4 \rightarrow ^3H_6$) [15], as observed in Fig. 5d. It is important to note that the emission lines
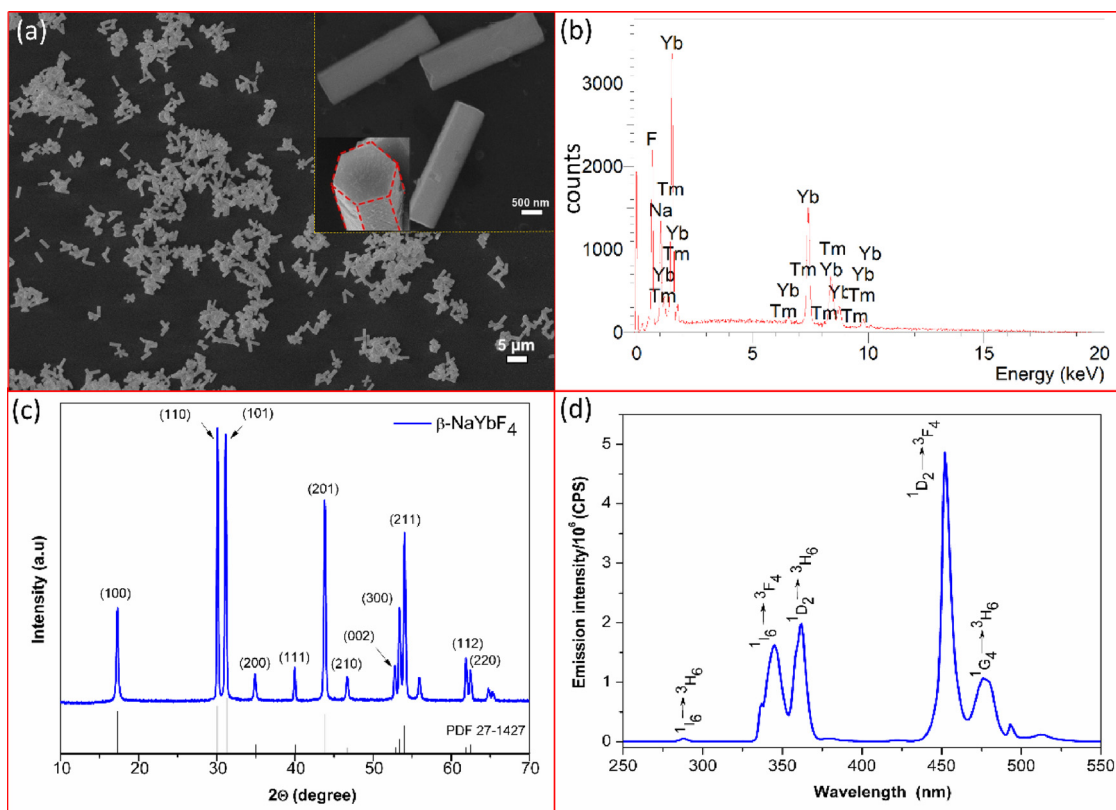
Fig. 5. (a) SEM image, (b) EDX spectrum (c) XRD pattern and (d) photoluminescence (PL) UC emission spectra under 980 nm laser (0.5 W) excitation of $NaYbF_4$: Tm^{3+} UCPs. The inset in **a** is a magnified view of UCPs.

below 500 nm have sufficient energy to cause photoexcitation of BV which has a band gap of around 2.6 eV (Fig. 6b) and thus allowing the BV/UCPs system to be photocatalytically active under NIR illumination (*vide infra*).

3.3. Photoactivity of BV under visible light and UV–vis light illumination

The photocatalytic activity of BV samples prepared under different conditions (pH, microwave treatment time) was evaluated by photodegradation of CV dye using blue-emitting (460 nm) LEDs as visible radiation source and xenon/Hg lamp as UV–vis radiation source. In the absence of BV samples, no obvious decrease in the CV absorption peak was observed indicating that direct photolysis (DP) of CV by the LEDs light was negligible (DP in Fig. 7a and c). In the presence of BV samples, however, a remarkable decrease in the characteristic absorption peak of CV (Fig. S10a) occurs after exposing the CV/BV mixture to visible light,
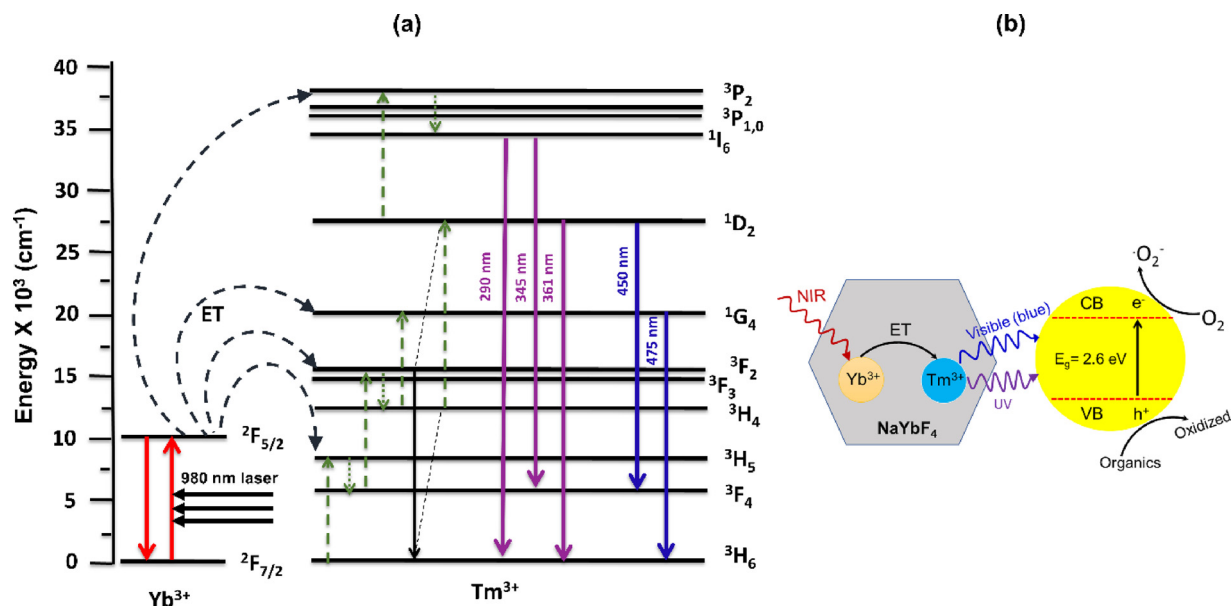

Fig. 6. (a) Upconversion mechanism of Tm^{3+} doped $NaYbF_4$ UCPs under 980 nm laser excitation and (b) schematic representation the mechanism of NIR-driven photocatalytic activity of the BV/UCPs photocatalytic system.
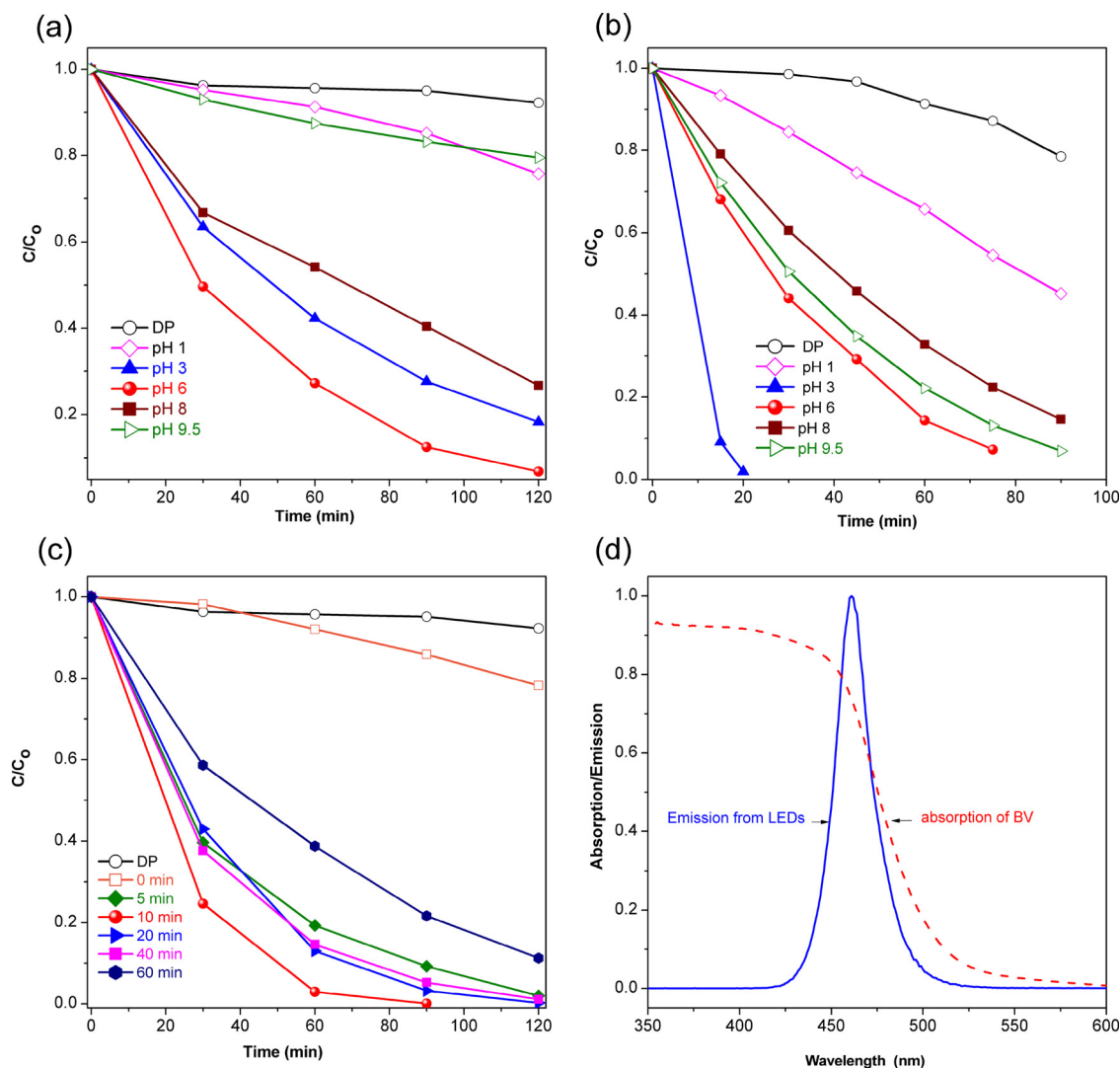
Fig. 7. The decrease in concentration of CV as function of irradiation time in the absence (direct photolysis, DP) and presence of BV samples prepared at different pH using (a) visible light from LED and (b) UV–vis light from xenon lamp; (c) the decrease in concentration of CV as function of visible light (LEDs) irradiation time in the presence of BV samples prepared using different microwave treatment times; (d) optical spectra showing the overlap between the emission spectrum of LEDs source and absorption spectrum of BV (pH6) sample.

confirming the visible light photoactivity of BV samples. The LEDs-based visible light activity could be attributed to an almost complete overlap between the emission spectrum of blue LEDs and absorption spectrum of the monoclinic BV sample (Fig. 7d). Such perfect overlap makes it possible for the monoclinic BV to effectively absorb most of the emitted light from LEDs and consequently good photocatalytic activity of the BV samples was observed despite the low power (total electric power = 1.26 W, light intensity output at 460 nm = 2.5 mW/cm^2) of the LEDs employed.

The visible light photoactivity of the BV sample was found to be strongly dependent on the pH of the reaction medium used during synthesis (Fig. 7a) and to a little extent on the microwave treatment time (Fig. 7c) used in the synthesis of the samples. The values of rate constant (k_{obs}) for different BV samples as measured by photocatalytic degradation of CV are reported in Table 1. For the samples prepared at different pH, the visible light photoactivity was found to be highest for BV(pH6) sample and lowest for BV(pH1) and BV(pH9.5) samples. The BV(pH6) sample photodegraded around 84% of the CV dye within 2 h of visible light irradiation (k_{obs} = 0.023 min^{-1}). Such higher visible light photoactivity of this sample may be related to its smaller particle dimensions (Fig. 1) and small crystallite size (Table S1) and the presence of almost phase-pure monoclinic BV (Fig. 3b and Table 1) which

effectively absorbs visible light. In general, samples with hyper-branched morphology and nanometric dimensions (pH 3, 6 and 8) exhibit higher photoactivity than samples with bigger particles (pH 1 and 9.5). The slightly higher visible light activity of BV (pH3) than BV(pH 8) may be related to the presence of monoclinic/tetragonal heterojunction (as discussed later) or the presence of particles with smaller dimensions. Knowing that the monoclinic scheelite phase of BV has higher visible light photoactivity than its tetragonal counterparts [82], BV samples (pH 3, 6 and 8) which contain monoclinic as the predominant phase show better photocatalytic response than those consisting of tetragonal phase (pH 1 and 9.5) under visible light illumination.

Interestingly, however, the photocatalytic behavior of the samples and the relationship of photoactivity with phase composition and optical properties is strongly dependent on the illumination mode (visible vs. UV–vis light). For instance, the lower visible light photoactivity of BV(pH 9.5) sample (Fig. 7a) may be directly related to the presence of 90.5% tetragonal phase (see Fig. 3b) with higher band gap (E_g ~2.93 eV, Fig. 4b) [83]. Due to its higher band gap (E_g ~2.93 eV), it significantly absorbs in the UV region and consequently exhibits low photoactivity in the visible region. In other words, since the optical properties of samples prepared at different pH are different (Fig. 4), the greater degree of overlap between the emission spectrum of the LEDs

and absorption spectra of some samples (pH6, for instance) as compared to other samples (*e.g.*, pH9.5) might also lead to a difference in photoactivity of the samples. The situation becomes different, however, when we switch from visible (LEDs) to UV–vis (xenon/Hg lamp) illumination. In the presence of UV–vis light, both the tetragonal (E_g = 2.9 eV) and monoclinic (E_g = 2.6 eV) phases could be photoexcited. A comparison of the photoactivity of the samples under visible LED illumination (Fig. 7a) and UV–vis illumination (Fig. 7b) indicates marked differences in the photocatalytic response of the samples (see k_{obs} values in Table 1, also). All samples (pH 1, 3 and 9.5) consisting of mixed phases (monoclinic + tetragonal) show a larger increase in photoactivity than that observed in BV sample with pure monoclinic phase (pH6, for instance), when irradiated with UV–vis light. The increase in photoactivity under UV–vis illumination is more drastic in case of BV(pH3) sample consisting of around 68% monoclinic and 30% tetragonal phase, as indicated by an almost 12 times increase in the observed rate constant (k_{obs}) for photodegradation of CV under otherwise identical conditions (Table 1). Such pronounced enhancement in photoactivity may be attributed to the two distinct, though related, factors: (i) simultaneous photoexcitation of total photocatalysts amount (both tetragonal and monoclinic phase) under UV–vis illumination and/ or (ii) the formation of monoclinic/tetragonal heterojunction [37,39,42,48] which we verified through simple switching of the illumination mode from purely visible (LEDs) to UV–vis (xenon/Hg lamp) (Fig. 7a *vs.* b). Considering factor 1, an increase in photoactivity may simply arise from the fact that, using UV–vis illumination, the tetragonal phase also becomes photoactive, and the observed photoactivity has contribution from both monoclinic and tetragonal phase. Considering factor 2, the formation of monoclinic/tetragonal heterojunction has been reported to increase the photoactivity of BV due to

improved interfacial charge transfer (see Fig. 8c) and lower charge carrier recombination [37,39,42,48].

To verify the effect of phase composition and monoclinic/tetragonal heterojunction on photoactivity, the k_{obs} values (Table 1) of all samples were normalized by rate constant (k_T) of predominantly tetragonal BV (k_T = 0.002 and 0.024 min^{-1} for visible and UV–vis illumination, respectively) [65]. The normalized rate constants (K = k_{obs}/k_T) are plotted as function of the content of monoclinic BV in Fig. 8 for both visible and UV–vis illumination. Fig. 8a shows that, under UV–vis illumination, both pure monoclinic and predominantly tetragonal BV show lower K values as compared to a sample (BV(pH 3)) containing ~ 68% monoclinic and ~ 30% tetragonal phase. Such higher activity of this heterophase sample results from a synergetic effect associated with the formation of monoclinic/tetragonal heterojunction [37,39,42,48]. Such synergic effect on photoactivity has also been observed in heterophase titania consisting of in anatase/rutile mixture [65].

Using X-ray photoelectron spectroscopy, Li et al. studied the valence band position of different polymorphs of BV and found a value of 0.9 eV and 1.1 eV for tetragonal and monoclinic BV, respectively [83]. Moreover, they found that the difference in band structure of tetragonal and monoclinic BV originates from the difference in the valence top. Lopes and coworkers, however, found that the valence band top of heterophase BV with monoclinic/tetragonal heterojunction was much higher (+2 eV) than pure monoclinic (+1.1 eV) or pure tetragonal (+0.9 eV) BV, indicating that the formation of monoclinic/tetragonal heterojunction resulted in a shift in the valance band top of BV [39]. Thus, owing to the suitable position of valence and conduction bands of the two phases and the formation of a monoclinic/tetragonal heterojunction [39], an interfacial transfer of charge carries (e$^-$ and h$^+$) between these two phases is possible [39], as depicted in Fig. 8c. Such interfacial
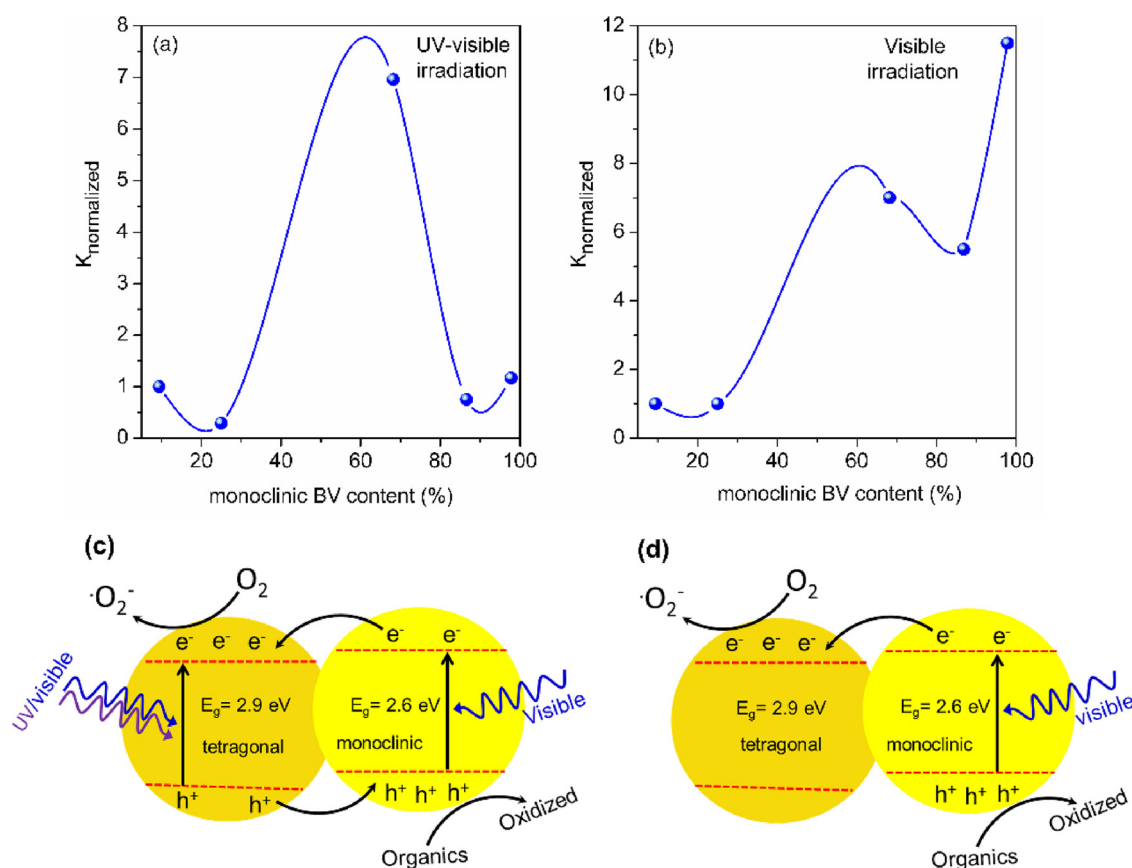

Fig. 8. The normalized rate constant (K = k_{obs}/k_T) plotted as function of the content (%) of monoclinic BV for photocatalytic degradation of CV in the presence of different BV samples under (a) UV–vis illumination and (b) visible illumination and schematic representation of the monoclinic/tetragonal heterojunction in BV showing interfacial transfer of charge carries (electrons and holes) under (c) UV/visible light irradiation and (d) visible illumination.
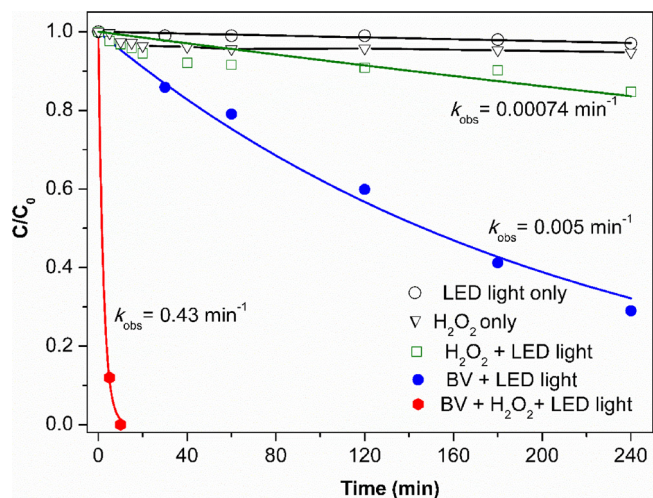
Fig. 9. The change in concentration of STZ as function of visible light illumination time (min) from LEDs in the presence of only BV (●) and BV plus 1.5 mmol L^{-1} H_2O_2 (●). Experimental controls including degradation of STZ by direct photolysis (○), H_2O_2 (1.5 mmol L^{-1}) in dark (▽) and H_2O_2 (1.5 mmol L^{-1}) under LED light (□) are also shown for comparison.

charge transfer can lower the recombination of charge carries (Fig. S11) [48] and leads to a synergic enhancement in the photoactivity of mixed-phase BV samples (see Figs. 7b and 8 c) [37,39,42].

To further support this hypothesis and compare the separation efficiency of the photoinduced charge carriers, the PL emission intensity resulting from radiative recombination of charge carriers was measured under 375 nm excitation. The PL emission intensity is the lowest for BV (pH3) sample (Fig. S11). The lower emission intensity of BV(pH3) indicates a better charge carrier separation (lower recombination) in this sample due to the presence of monoclinic/tetragonal heterojunction [37,39,42] (Fig. 8c and d) and hence this sample showed the highest photoactivity under UV–vis irradiation (Figs. 7b and S10b). The TOC removal efficiency of this BV(pH3) sample under UV–vis illumination was also the highest (> 73%). TOC removal efficiency of 3, 59 and 67.8% was obtained in case of BV(pH1), BV(pH6) and BV(pH 8), respectively.

To verify the role of phase composition or heterojunction formation on the photocatalytic efficiency under visible light illumination, the normalized rate constants (K) for photocatalytic degradation of CV under visible light were also plotted as function of the content of monoclinic BV (Fig. 8b). It is clear that, under visible light illumination from LEDs, the K values roughly increase with increase in the content of monoclinic BV. However, an unexpected region of higher activity (higher K value) is again observed for sample with 68% monoclinic and 30% tetragonal BV (BV(pH3) sample). This also explains why BV(pH3) shows slightly higher visible light photoactivity than BV(pH 8) sample (Fig. 7a) despite having lower monoclinic content. The phase composition and formation of heterojunction thus seems to determine the photocatalytic efficiency even under visible light illumination. In case of visible light illumination, the role of heterojunction seems to be related to a possible transfer of electrons from conduction band of monoclinic BV to conduction band of tetragonal BV, thereby decreasing the e^-–h^+ recombination in monoclinic BV (Fig. 8d). On the other hand, under UV–vis irradiation, in addition to a transfer of conduction band electrons from the monoclinic to tetragonal phase, the transfer of holes between their valence bands in the opposite direction is also possible (Fig. 8c). Thus, the effect of heterojunction becomes more important under UV–vis illumination as compared to only visible illumination.

Moreover, it is well-known that the photocatalytic activity of semiconductor materials depends on their microstructure (particle morphology, size, shape and surface texture) and phase or crystalline

structure (which in turn affects the electronic structure and hence the mobility of photogenerated charge carriers). Thus, one obvious reason for this similarity in photoactivity of BV sample prepared using different microwave treatment times (Fig. 7c) seems to be related to their closely matching E_g values and hence identical optical properties (Fig. S8) as well as their similar phase composition (97 ± 2% monoclinic BV) (Table 1). Among this set of BV samples prepared using different microwave treatment times, however, some slight differences in photocatalytic activity are observed. The sample prepared without microwave-assisted hydrothermal treatment (0 min) exhibits very low photoactivity ($k_{obs} = 0.0017 min^{-1}$), emphasizing the role of microwave treatment in obtaining BV samples with controlled morphology (Fig. S1), crystallinity (Fig. S4) and optical properties (Fig. S8a). Crystallinity of samples is important since it affects the electronic structure and optical behavior of the photocatalyst as well as the recombination or transport of photogenerated charge carriers. Since well-crystalline BV samples are obtained upon microwave treatment (Fig. S4), they exhibit good visible light photoactivity (Fig. 7c). In fact, a microwave treatment for as short as 5 min is enough to obtain photoactive samples. The BV(10 min) sample prepared using 10 min microwave irradiation exhibits the smallest particle dimension (Fig. S1) and crystallite size (35.7 nm, Table S1) and less aggregation and consists of phase-pure monoclinic scheelite phase with no traces of tetragonal phase. Consequently, this sample exhibits the highest photoactivity and almost 100% photodegradation of CV was observed after 90 min of visible light irradiation (k_{obs} ~ 0.05 min^{-1}). The visible light photoactivity decreases slightly upon microwave treatment longer than 10 min which may be related to the presence of tetragonal phase (as witnessed by the XRD analysis (Table 1) and/or the slight increase in particle size, crystallite sizes (Table S1) and aggregation, most probably following a dissolution-precipitation mechanism [15] during the microwave-assisted hydrothermal treatment.

The photoactivity of the BV(pH6) sample under LEDs illumination was also tested by photodegradation of STZ as model pharmaceutical drug. Control experiments (in absence of BV) using only LED illumination (direct photolysis), H_2O_2 in dark and H_2O_2 along with LED illumination show an STZ photodegradation of 3%, 6% and 15%, respectively (Fig. 9). In the presence of BV, however, a steady decrease in concentration of STZ is observed with increase in LEDs illumination time and 71% of STZ was photodegraded in 4 h at a rate of 0.005 min^{-1}. Moreover, about 86 times increase in photodegradation rate (k_{obs} = 0.43 min^{-1}) is achieved by addition of as small as 1.5 mmol L^{-1} H_2O_2 to the BV/STZ mixture and 100% photodegradation of STZ is observed within 10 min of visible light illumination from LEDs. These results highlight the importance of the developed photocatalytic system as an effective system for wastewater treatment.

An important aspect of any photocatalyst is its stability and recyclability. We thus tested the photocatalytic efficiency, recyclability and stability of BV photocatalysts after three repeated photocatalytic cycles (Fig. S12). The amount of CV dye photodegraded after 2 h of LED illumination was 94.3%, 75% and 73% for the first, second and third cycles, respectively (Fig. S12a). Similarly, the total organic carbon (TOC) removal efficiency was 49%, 45% and 42% for the first, second and third cycles, respectively (Fig. S12b). Moreover, since no significant change in the particle morphology (Fig. S13) or crystalline structure (Fig. S14) of the BV photocatalysts is observed after three repeated cycles of use, it can be assumed that the little loss in photoactivity (Fig. S12) resulted from the less efficient recovery or loss of the photocatalysts material during centrifugation.

3.4. Solar light photoactivity of BV

After the photocatalytic tests under controlled illumination using LEDs and establishing some structure-photoactivity relationships, the photoactivity of the prepared BV samples under natural sunlight illumination (light intensity output = 17.4 and 33.6 mW/cm^2 at 460 and
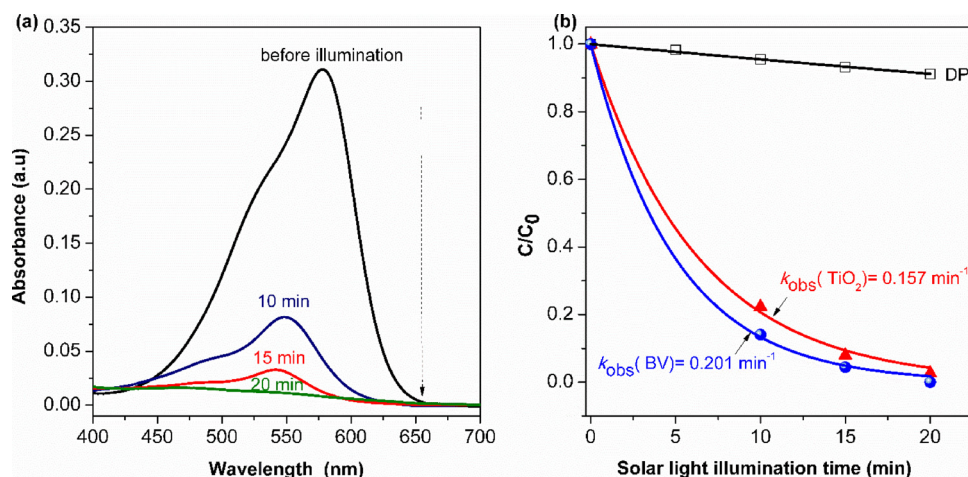
Fig. 10. (a) Absorption spectra of CV dye solution after exposure to natural sunlight irradiation for different length of time in the presence of BV(10 min) photocatalyst and (b) the decrease in concentration of CV dye as function of sunlight illumination time in presence of BV and TiO_2 (P25) photocatalysts. Direct photolysis of CV dye is also shown for comparison.

365 nm, respectively) was also evaluated by the photodegradation of CV and STZ. Fig. 10a shows that the absorption peak of CV decreases sharply upon exposure of the CV/BV mixture to natural sunlight illumination indicating high solar-light driven photocatalytic activity of the prepared BV photocatalyst. As shown in Fig. 10b, almost 100% of the dye is photobleached within 20 min of sunlight illumination with an observed rate constant of 0.20 min^{-1} which is slightly higher than that of commercial P25 TiO_2 ($k_{obs} = 0.157$ min^{-1}) measured under identical condition (Fig. 10b) and much higher than LEDs-based illumination ($k_{obs} = 0.048$ min^{-1}). The photoactivity of BV(10 min) sample in natural sunlight and LEDs illumination under otherwise same experimental conditions are also compared in Fig. S15 and the prepared BV samples show far superior photoactivity towards degradation of CV under sunlight illumination as compared to LEDs illumination due to higher visible light intensity of the former. Similarly, the BV could effectively photodegrade around 58% of STZ molecules under natural solar light illumination for 3 h (Fig. S16). While the higher solar-driven photoactivity is important for effective harvesting of sunlight for photochemical reactions during daytime, the LEDs-based photoactivation is important for photocatalytic reactions during the night time and for evaluating the role of experimental conditions on the photocatalytic behavior of the system in a controlled manner.

3.5. NIR-based photoactivity of BV/NaYbF₄:Tm³⁺ photocatalytic system

The NIR-based photoactivity of UCPs/BV mixture under 980 nm laser excitation was studied through photodegradation of CV and STZ solution. As shown in Fig. 11a, the emission spectrum of NaYbF₄:Tm³⁺ UPCs and the absorption spectrum of BV (monoclinic) show a good overlap in the region blow 500 nm, and it could be reasonably inferred that the NIR-to-UV/visible upconverted light from UCPs could be effectively used to photoexcite BV, especially in monoclinic phase. To confirm this hypothesis, we followed the evolution of absorption spectra of CV dye as function of NIR irradiation time. The direct photolysis (DP) of CV by laser irradiation in the absence of any photocatalysts and the photodegradation of CV in the presence of only BV (absence of UCPs) are smaller under the experimental conditions (Fig. 11c). Upon exposure of the UCPs/BV/CV mixture to NIR radiation from a laser, however, a clear decrease in the CV absorption peak (Fig. 11b) is observed which confirms the photoexcitation of BV by the UC emission from UCPs. As a result of photoexcitation, oxidative h⁺ and reductive e⁻ are generated. The reductive e⁻ and oxidative h⁺ react with molecular O_2 and water to ultimately result in the formation of ˙OH radicals which, together with direct oxidation by h⁺ formed in the valence band, cause photodegradation of CV dye (Fig. 11b) [39]. As a result, in the presence of UCPs/BV mixture, the concentration of CV shows a steady decrease with increase in NIR illumination time and

around 80% of the CV dye is photodegraded within 6 h of NIR irradiation (Fig. 11c). For comparison, the photodegradation of CV in the presence of UCPs and commercial P25 TiO_2 was also studied under identical experimental condition (Fig. 11c, red line). It is clear from Fig. 11c that the UCPs/BV mixture ($k_{obs} = 0.3$ h^{-1}) shows a higher photoactivity than UCPs/TiO_2 ($k_{obs} = 0.1$ h^{-1}) under NIR illumination. This difference in NIR photoactivity may be explained considering that the UCPs/TiO_2 system [28,31,65] harvests only a smaller and less intense UV portion ($E_g = 3.2$ eV for TiO_2) of the total upconversion emission while the BV in UCPs/BV system, in principle, can absorb a wider portion (UV/visible) of the upconverted light.

To further confirm the photoactivation of BV with upconverted photons from the UCPs, we employed terephthalic acid as a probe molecule [66]. Terephthalic acid reacts with ˙OH radicals to form 2-hydroxyterephthalic acid with enhanced fluorescence emission centred at around 425 nm when excited at 315 nm. As presented in Fig. 11d, a comparison of the fluorescence intensity of terephthalic acid before and after exposure to NIR radiation (980 nm) in the presence of BV/NaYbF₄:Tm³⁺ indicates a clear increase in fluorescence intensity which confirms the formation of ˙OH radicals and hence the photoactivation of BV by the NIR-to-UV/visible upconverted emission from UCPs. For BV, both direct (photooxidation of organic molecules by the oxidative h⁺) and indirect (involving ˙OH and ⁻˙O₂ radicals) mechanisms of photodegradation have been reported [39]. Our results also indicated the formation of ˙OH radicals as active species (Fig. 11d). Through controlled experiment using a variety of scavengers of ˙OH radical, conduction band e⁻ or ⁻˙O₂ and valence band h⁺, Lopes et al. concluded that the direct mechanism play a major role in photocatalytic degradation of organic molecules by heterophase BV samples, through the overall efficiency of photocatalytic degradation depends on both direct and indirect mechanism [39].

We also studied the photodegradation of STZ molecules under 980 nm NIR illumination in the absence (DP) and presence of UCPs/BV photocatalyst (Fig. S17). First, we tested the photodegradation of STZ through direct photolysis by the laser irradiation (in the absence of any photocatalysts) which was found to be smaller (5%). In the presence of UCPs/BV mixture, however, around 28% photodegradation of STZ was observed upon NIR illumination for 6 h (Fig. S17), confirming the reasonably good photoactivity of the BV/UCPs system towards photodegradation of pharmaceutical molecules.

The mechanism of NIR-based photocatalysis of the BV/UCPs system is shown in Fig. 6b. As explained earlier, the Yb³⁺ ions absorb the laser radiation (980 nm) and get excited. Subsequent multistep ET to Tm³⁺ ions excite the later which, upon relaxation, emit the upconverted radiation in the UV region (290, 345, 361 nm) and visible region (450, 475 nm (blue region)) [15] (see Fig. 6a). Since the absorption edge of BV lies at round 500 nm (Fig. 11a), the upconverted radiation in the
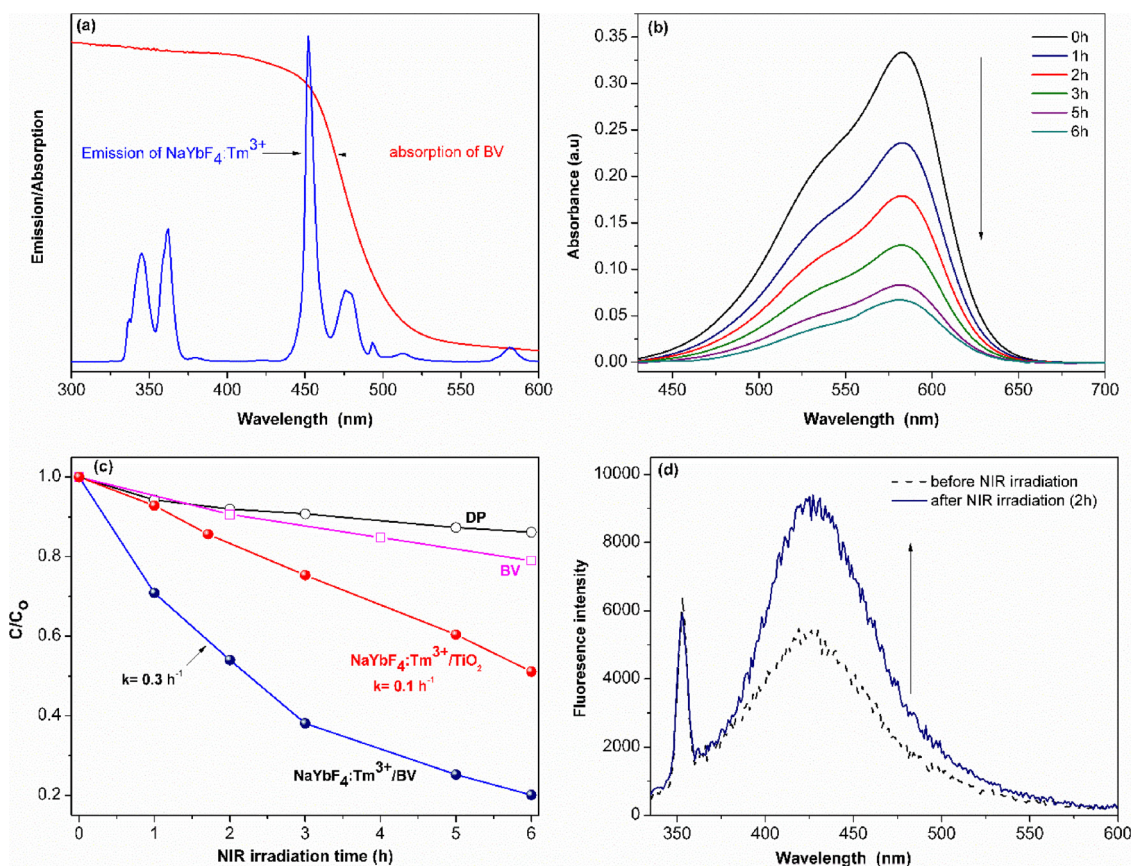
Fig. 11. (a) Optical spectra showing the overlap between the PL emission spectrum of NaYbF$_4$:Tm^{3+} UCPs (blue line) and absorption spectra of monoclinic BV (red line), (b) absorption spectra of CV dye solution after exposure to 980 nm NIR irradiation for different length of time in the presence of BV/UCPs photocatalyst, (c) the decrease in concentration of CV as function of NIR irradiation time in the absence (DP) of any photocatalysts (○) and in the presence of BV only (□), BV/UCPS mixture (●) and P25 TiO$_2$/UCPs mixture (●) (d) comparison of the fluorescence intensity (λ_{exc} = 315 nm, λ_{em} = 425 nm) of terephthalic acid before and after exposure to NIR radiation (980 nm) in the presence of BV/NaYbF$_4$:Tm^{3+} (For interpretation of the references to colour in this figure legend, the reader is referred to the web version of this article).

blue and UV region could be absorbed by BV leading to its photo-activation with the subsequent formation of electron-hole (e$^-$–h$^+$) pairs. As explained earlier, these photogenerated oxidative h$^+$ and reductive e$^-$ as well as ·O$_2$ (formed as a result of capture of e$^-$ by dissolved oxygen) are responsible for the photocatalytic activity of BV photocatalysts [39] (see Fig. 6b). Coupling BV with UCPs can thus be considered one of the possible ways and general strategies to broaden the photocatalytic response range of BV (and other semiconductor photocatalysts) as the UCPs/BV photocatalyst can harvest both visible light (direct photoexcitation of BV) and NIR (indirect photoexcitation of BV through upconverted UV/visible light from UCPs under NIR excitation) for photochemical reactions.

4. Conclusions

In this study, two photocatalytic system (BV/LEDs and BV/UCPs) are introduced as a strategy for the photocatalytic degradation of both organic dyes and pharmaceuticals under a variety of photoactivation modes including low-power (1.26 W) LEDs and near infrared (NIR) irradiation as well as natural sunlight. The first system (BV/LED illumination) makes use of the perfect match between the emission of low-cost blue LEDs and absorption of BV since the LEDs emission matches the band gap energy of BV. The second one (BV/UCPs) exploits the NIR-to-UV/visible upconverted light from UCPs (NaYbF$_4$:Tm^{3+}) to allow photodegradation of pollutants under NIR illumination. Using a facile and rapid microwave-assisted hydrothermal method, we could obtain NaYbF$_4$:Tm^{3+} hexagonal UCPs and highly crystalline BV powder with tailored morphology, crystalline phase and band-gap energies

(2.4–2.93 eV). Among the experimental conditions, pH was found to strongly affect the structural, optical and hence photocatalytic properties of BV samples. While pure monoclinic phase exhibited higher activity under visible light (LEDs illumination), heterophase BV samples exhibited the highest photoactivity under UV–vis illumination due to the formation of a tetragonal/monoclinic heterojunction. It may be emphasized that while the visible-light activity of BV combined with the economical and practical LED-based illumination is important for application in photocatalytic remediation of pollutants in remote and isolated areas using low-power DC voltage sources, coupling of UCPs with BV and other narrow/wide band semiconductors may be regarded as a promising strategy to develop broad-spectrum photocatalysts for effective harvesting of solar light for photo(electrochemical) reactions.

Appendix A. Supplementary data

Supplementary material related to this article can be found, in the online version, at doi:https://doi.org/10.1016/j.apcatb.2018.09.091.

References

[1] WHO/UNICEF, Progress on Drinking Water, Sanitation and Hygiene: 2017 Update and SDG Baselines, (2017) https://www.unicef.org/publications/files/Progress_on_Drinking_Water_Sanitation_and_Hygiene_2017.pdf.

[2] A.J. Expósito, J.M. Monteagudo, A. Durán, I. San Martín, L. González, Study of the intensification of solar photo-Fenton degradation of carbamazepine with ferrioxalate complexes and ultrasound, J. Hazard. Mater. 342 (2018) 597–605, https://doi.org/10.1016/j.jhazmat.2017.08.069.

[3] H. Wang, Y. Liang, L. Liu, J. Hu, W. Cui, Highly ordered TiO2 nanotube arrays wrapped with g-C3N4 nanoparticles for efficient charge separation and increased photoelectrocatalytic degradation of phenol, J. Hazard. Mater. 344 (2018) 369–380, https://doi.org/10.1016/j.jhazmat.2017.10.044.

[4] O. Legrini, E. Oliveros, a.M. Braun, Photochemical processes for water treatment, Chem. Rev. 93 (1993) 671–698, https://doi.org/10.1021/cr00018a003.

[5] C. Comninellis, A. Kapalka, S. Malato, S.A. Parsons, I. Poulios, D. Mantzavinos, Advanced oxidation processes for water treatment: advances and trends for R&D, J. Chem. Technol. Biotechnol. 83 (2008) 769–776, https://doi.org/10.1002/jctb.1873.

[6] S. Ullah, E.P. Ferreira-Neto, A.A. Pasa, C.C.J. Alcântara, J.J.S. Acuña, S.A. Bilmes, M.L. Martínez Ricci, R. Landers, T.Z. Fermino, U.P. Rodrigues-Filho, Enhanced photocatalytic properties of core@shell SiO2@TiO2 nanoparticles, Appl. Catal. B Environ. 179 (2015) 333–343, https://doi.org/10.1016/j.apcatb.2015.05.036.

[7] V. Likodimos, Photonic crystal-assisted visible light activated TiO2 photocatalysis, Appl. Catal. B Environ. 230 (2018) 269–303, https://doi.org/10.1016/j.apcatb.2018.02.039.

[8] M.N. Chong, B. Jin, C.W.K. Chow, C. Saint, Recent developments in photocatalytic water treatment technology: a review, Water Res. 44 (2010) 2997–3027, https://doi.org/10.1016/j.watres.2010.02.039.

[9] K. Nakata, A. Fujishima, TiO2 photocatalysis: design and applications, J. Photochem. Photobiol. C Photochem. Rev. 13 (2012) 169–189, https://doi.org/10.1016/j.jphotochemrev.2012.06.001.

[10] R. López, R. Gómez, Band-gap energy estimation from diffuse reflectance measurements on sol–gel and commercial TiO2: a comparative study, J. Sol-Gel Sci. Technol. 61 (2012) 1–7, https://doi.org/10.1007/s10971-011-2582-9.

[11] K. Hashimoto, H. Irie, A. Fujishima, TiO2 photocatalysis: a historical overview and future prospects, Jpn. J. Appl. Phys. 44 (2005) 8269–8285, https://doi.org/10.1143/JJAP.44.8269.

[12] M.P. Vincenzo Augugliaro, Vittorio Loddo, Giovanni Palmisano, Leonardo Palmisano, Clean by Light Irradiation: Practical Applications of Supported TiO2, The Royal Society of Chemistry, Cambridge, UK, 2010.

[13] S. Devipriya, S. Yesodharan, Photocatalytic degradation of pesticide contaminants in water, Sol. Energy Mater. Sol. Cells 86 (2005) 309–348, https://doi.org/10.1016/j.solmat.2004.07.013.

[14] A. Wold, Photocatalytic properties of TiO2, Chem. Mater. 5 (1993) 280–283.

[15] S. Ullah, C. Hazra, E.P. Ferreira-Neto, T.C. Silva, U.P. Rodrigues-Filho, S.J.L. Ribeiro, Microwave-assisted synthesis of NaYF4:Yb 3 + /Tm 3 + upconversion particles with tailored morphology and phase for the design of UV/NIR-active NaYF 4 :Yb 3 + /Tm 3 + @TiO 2 core@sh, CrystEngComm 19 (2017) 3465–3475, https://doi.org/10.1039/C7CE00809K.

[16] A.L. Linsebigler, G. Lu, J.T. Yates Jr, J.T. Yates, Photocatalysis on TiO2 surfaces: principles, mechanisms, and selected results, Chem. Rev. 95 (1995) 735–758, https://doi.org/10.1021/cr00035a013.

[17] A. Ayati, A. Ahmadpour, F.F. Bamoharram, B. Tanhaei, M. Mänttäri, M. Sillanpää, A review on catalytic applications of Au/TiO2 nanoparticles in the removal of water pollutant, Chemosphere 107 (2014) 163–174, https://doi.org/10.1016/j.chemosphere.2014.01.040.

[18] A. Bumajdad, M. Madkour, Understanding the superior photocatalytic activity of noble metals modified titania under UV and visible light irradiation, Phys. Chem. Chem. Phys. 16 (2014) 7129–7628, https://doi.org/10.1039/c3cp54411g.

[19] Á. Veres, T. Rica, L. Janovák, M. Dömök, N. Buzás, V. Zöllmer, T. Seemann, a. Richardt, I. Dékány, Silver and gold modified plasmonic TiO2 hybrid films for photocatalytic decomposition of ethanol under visible light, Catal. Today 181 (2012) 156–162, https://doi.org/10.1016/j.cattod.2011.05.028.

[20] N. a Ramos-Delgado, M. a Gracia-Pinilla, L. Maya-Treviño, L. Hinojosa-Reyes, J.L. Guzman-Mar, a Hernández-Ramírez, Solar photocatalytic activity of TiO2 modified with WO3 on the degradation of an organophosphorus pesticide, J. Hazard. Mater. 263 (Pt. 1) (2013) 36–44, https://doi.org/10.1016/j.jhazmat.2013.07.058.

[21] A. Rey, P. García-Muñoz, M. Hernández-Alonso, E. Mena, S. García-Rodríguez, F. Beltrán, WO3–TiO2 based catalysts for the simulated solar radiation assisted photocatalytic ozonation of emerging contaminants in a municipal wastewater treatment plant effluent, Appl. Catal. B Environ. 154–155 (2014) 274–284, https://doi.org/10.1016/j.apcatb.2014.02.035.

[22] F. Riboni, L.G. Bettini, D.W. Bahnemann, E. Selli, WO3–TiO2 vs. TiO2 photocatalysts: effect of the W precursor and amount on the photocatalytic activity of mixed oxides, Catal. Today 209 (2013) 28–34, https://doi.org/10.1016/j.cattod.2013.01.008.

[23] S.A.K. Leghari, S. Sajjad, F. Chen, J. Zhang, WO3/TiO2 composite with morphology change via hydrothermal template-free route as an efficient visible light photocatalyst, Chem. Eng. J. 166 (2011) 906–915, https://doi.org/10.1016/j.cej.2010.11.065.

[24] C. Ying, D. Hao, W. Lishi, Doped-TiO2 photocatalysts and synthesis methods to prepare TiO2 films, J. Mater. Sci. Technol. 24 (2008) 675–689 (Accessed 27 March, 2014), http://d.wanfangdata.com.cn/periodical_clkxjsxb-e200805001.aspx.

[25] J. Lu, F. Su, Z. Huang, C. Zhang, Y. Liu, X. Ma, J. Gong, N-doped Ag/TiO2 hollow spheres for highly efficient photocatalysis under visible-light irradiation, RSC Adv. 3 (2013) 720, https://doi.org/10.1039/c2ra22713d.

[26] M. Pelaez, N.T. Nolan, S.C. Pillai, M.K. Seery, P. Falaras, A.G. Kontos, P.S.M. Dunlop, J.W.J. Hamilton, J.A. Byrne, K. O'Shea, M.H. Entezari, D.D. Dionysiou, A review on the visible light active titanium dioxide photocatalysts for environmental applications, Appl. Catal. B Environ. 125 (2012) 331–349, https://doi.org/10.1016/j.apcatb.2012.05.036.

[27] R. Asahi, Visible-light photocatalysis in nitrogen-doped titanium oxides, Science (80-.) 293 (2001) 269–271, https://doi.org/10.1126/science.1061051.

[28] W. Qin, D. Zhang, D. Zhao, K. Zheng, L. Wang, K. Zheng, Near-infrared photocatalysis based on YF3:Yb3 + ,Tm3 + /TiO2 core/shell nanoparticles, Chem. Commun. 46 (2010) 2304–2306, https://doi.org/10.1039/b924052g.

[29] X. Guo, W. Song, C. Chen, W. Di, W. Qin, Near-infrared photocatalysis of b-NaYF4:Yb3 + ,Tm3 + @ZnO composites, Phys. Chem. Chem. Phys. 15 (2013) 14681–14688, https://doi.org/10.1039/c3cp52248b.

[30] D.-X.X. Xu, Z.-W.W. Lian, M.-L.L. Fu, B. Yuan, J.W. Shi, H.-J.J. Cui, Advanced near-infrared-driven photocatalyst: fabrication, characterization, and photocatalytic performance of β-NaYF4: Yb3 + ,Tm3 + @TiO2 core@shell microcrystals, Appl. Catal. B Environ. 142–143 (2013) 377–386, https://doi.org/10.1016/j.apcatb.2013.05.062.

[31] Z. Yuewei, H. Zhanglian, Synthesis of lanthanide-doped NaYF4@TiO2 core–shell composites with highly crystalline and tunable TiO2 shells under mild conditions and their upconversionbased photocatalysis, Nanoscale 5 (2013) 8930–8933, https://doi.org/10.1039/c3nr03051b.

[32] X. Guo, W. Di, C. Chen, C. Liu, X. Wang, W. Qin, Enhanced near-infrared photocatalysis of NaYF 4 :Yb, Tm/CdS/TiO2 composites, Dalton Trans. 43 (2014) 1048–1054, https://doi.org/10.1039/C3DT52288A.

[33] G. Bin Shan, G.P. Demopoulos, Near-infrared sunlight harvesting in dye-sensitized solar cells via the insertion of an upconverter-TiO2 nanocomposite layer, Adv. Mater. 22 (2010) 4373–4377, https://doi.org/10.1002/adma.201001816.

[34] Z. Li, C. Li, Y. Mei, L. Wang, G. Du, Y. Xiong, Synthesis of rhombic hierarchical YF3 nanocrystals and their use as upconversion photocatalysts after TiO2 coating, Nanoscale 5 (2013) 3030–3036, https://doi.org/10.1039/c3nr34018j.

[35] Y.N. Tang, W.H. Di, X.S. Zhai, R.Y. Yang, W.P. Qin, NIR-responsive photocatalytic activity and mechanism of NaYF4:Yb,Tm@TiO2 core-shell nanoparticles, ACS Catal. 3 (2013) 405–412, https://doi.org/10.1021/Cs300808r.

[36] Y. Deng, L. Tang, C. Feng, G. Zeng, J. Wang, Y. Zhou, Y. Liu, B. Peng, H. Feng, Construction of plasmonic Ag modified phosphorous-doped ultrathin g-C3N4 nanosheets/BiVO4 photocatalyst with enhanced visible-near-infrared response ability for ciprofloxacin degradation, J. Hazard. Mater. 344 (2018) 758–769, https://doi.org/10.1016/j.jhazmat.2017.11.027.

[37] Y. Lee, M. Cui, J. Choi, J. Kim, Y. Son, J. Khim, Degradation of polychlorinated dibenzo-p-dioxins and dibenzofurans in real-field soil by an integrated visible-light photocatalysis and solvent migration system with p-n heterojunction BiVO4/Bi2O3, J. Hazard. Mater. 344 (2018) 1116–1125, https://doi.org/10.1016/j.jhazmat.2017.12.002.

[38] S.I. Eda, M. Fujishima, H. Tada, Low temperature-synthesis of BiVO 4 nanorods using polyethylene glycol as a soft template and the visible-light-activity for copper acetylacetonate decomposition, Appl. Catal. B Environ. 125 (2012) 288–293, https://doi.org/10.1016/j.apcatb.2012.05.038.

[39] O.F. Lopes, K.T.G.G. Carvalho, A.E. Nogueira, W. Avansi, C. Ribeiro, Controlled synthesis of BiVO4 photocatalysts: evidence of the role of heterojunctions in their catalytic performance driven by visible-light, Appl. Catal. B Environ. 188 (2016) 87–97, https://doi.org/10.1016/j.apcatb.2016.01.065.

[40] S. Sun, W. Wang, S. Zeng, M. Shang, L. Zhang, Preparation of ordered mesoporous Ag/WO3 and its highly efficient degradation of acetaldehyde under visible-light irradiation, J. Hazard. Mater. 178 (2010) 427–433, https://doi.org/10.1016/j.jhazmat.2010.01.098.

[41] Z.-F. Huang, L. Pan, J.-J. Zou, X. Zhang, L. Wang, Nanostructured bismuth vanadate-based materials for solar-energy-driven water oxidation: a review on recent progress, Nanoscale 6 (2014) 14044–14063, https://doi.org/10.1039/C4NR05245E.

[42] F.Q. Zhou, J.C. Fan, Q.J. Xu, Y.L. Min, BiVO4 nanowires decorated with CdS nanoparticles as Z-scheme photocatalyst with enhanced H2 generation, Appl. Catal. B Environ. 201 (2017) 77–83, https://doi.org/10.1016/j.apcatb.2016.08.027.

[43] N. Aiga, Q. Jia, K. Watanabe, A. Kudo, T. Sugimoto, Y. Matsumoto, Electron-phonon coupling dynamics at oxygen evolution sites of visible-light-driven photocatalyst: bismuth vanadate, J. Phys. Chem. C 117 (2013) 9881–9886, https://doi.org/10.1021/jp4013027.

[44] Y. Park, K.J. McDonald, K.-S. Choi, Progress in bismuth vanadate photoanodes for use in solar water oxidation, Chem. Soc. Rev. 42 (2013) 2321–2337, https://doi.org/10.1039/C2CS35260E.

[45] Y. Wang, F. Liu, Y. Hua, C. Wang, X. Zhao, X. Liu, H. Li, Microwave synthesis and photocatalytic activity of Tb(3 +) doped BiVO4 microcrystals, J. Colloid Interface Sci. 483 (2016) 307–313, https://doi.org/10.1016/j.jcis.2016.08.048.

[46] Y. Zhang, H. Gong, Y. Zhang, K. Liu, H. Cao, H. Yan, J. Zhu, The controllable synthesis of octadecahedral BiVO4 with exposed {111} facets, Eur. J. Inorg. Chem. (2017) 2990–2997, https://doi.org/10.1002/ejic.201700165.

[47] K. Pingmuang, A. Nattestad, W. Kangwansupamonkon, G.G. Wallace, S. Phanichphant, J. Chen, Phase-controlled microwave synthesis of pure monoclinic BiVO4 nanoparticles for photocatalytic dye degradation, Appl. Mater. Today 1 (2015) 67–73, https://doi.org/10.1016/j.apmt.2015.09.003.

[48] J. Safaei, H. Ullah, N.A. Mohamed, M.F. Mohamad Noh, M.F. Soh, A.A. Tahir, N. Ahmad Ludin, M.A. Ibrahim, W.N.R. Wan Isahak, M.A. Mat Teridi, Enhanced photoelectrochemical performance of Z-scheme g-C3 N4/BiVO4 photocatalyst,

Appl. Catal. B Environ. 234 (2018) 296–310, https://doi.org/10.1016/j.apcatb.2018.04.056.

[49] Z. Zhu, J. Du, J. Li, Y. Zhang, D. Liu, An EDTA-assisted hydrothermal synthesis of BiVO 4 hollow microspheres and their evolution into nanocages, Ceram. Int. 38 (2012) 4827–4834, https://doi.org/10.1016/j.ceramint.2012.02.071.

[50] B.J. Yu, A. Kudo, Effects of structural variation on the photocatalytic performance of hydrothermally synthesized BiVO4, Adv. Funct. Mater. (2006) 2163–2169, https://doi.org/10.1002/adfm.200500799.

[51] F. Wang, X. Liu, Recent advances in the chemistry of lanthanide-doped upconversion nanocrystals, Chem. Soc. Rev. 38 (2009) 976, https://doi.org/10.1039/b809132n.

[52] S. Wang, H. Zhang, Foundation of up-conversion nanoparticles, in: R. Liu (Ed.), Phosphors, Up Convers. Nano Part. Quantum Dots Their Appl. Springer, Singapore, Singapore, 2016, pp. 437–471, , https://doi.org/10.1007/978-981-10-1590-8.

[53] A. Francüois, Upconversion and anti-stokes processes with f and d ions in solids, Chem. Rev. 104 (2004) 139–173, https://doi.org/10.1021/cr020357g.

[54] J.P. Ghosh, C.H. Langford, G. Achari, Characterization of an LED based photoreactor to degrade 4-chlorophenol in an aqueous medium using coumarin (C-343) sensitized TiO2, J. Phys. Chem. A 112 (2008) 10310–10314, https://doi.org/10.1021/jp804356w.

[55] L. Yu, G. Achari, C.H. Langford, LED-based photocatalytic treatment of pesticides and chlorophenols, J. Environ. Eng. 139 (9) (2013) 1146–1151, https://doi.org/10.1061/(ASCE)EE.1943-7870.0000730.

[56] M. Izadifard, G. Achari, C. Langford, Application of photocatalysts and LED light sources in drinking water treatment, Catalysts 3 (2013) 726–743, https://doi.org/10.3390/catal3030726.

[57] A.Y.S. Malkhasian, M. Izadifard, G. Achari, C.H. Langford, Photocatalytic degradation of agricultural antibiotics using a UV-LED light source, J. Environ. Sci. Health B 49 (2014) 35–40, https://doi.org/10.1080/03601234.2013.836871.

[58] P. Nickels, H. Zhou, S.N. Basahel, A.Y. Obaid, T.T. Ali, A.A. Al-Ghamdi, E.-S.H. El-Mossalamy, A.O. Alyoubi, S.A. Lynch, Laboratory scale water circuit including a photocatalytic reactor and a portable in-stream sensor to monitor pollutant degradation, Ind. Eng. Chem. Res. 51 (2012) 3301–3308, https://doi.org/10.1021/ie202366m.

[59] M. Rasoulifard, M. Fazli, M. Eskandarian, Kinetic study for photocatalytic degradation of Direct Red 23 in UV–LED/nano-TiO2/S2O82− process: dependence of degradation kinetic on operational parameters, J. Ind. Eng. Chem. 20 (2014) 3695–3702, https://doi.org/10.1016/j.jiec.2013.12.068.

[60] J.F. Possatto, Desenvolvimento De Um Reator Fotoquímico Microcontrolado, Utilizando Diodos Emissores De Luz (Leds) Como Fonte De Excitação Luminosa, file:///E:/Postdoc 2016/Refrences/Reactor designs/LEDS reazctor UFSCAr.pdf, (2011) https://repositorio.ufscar.br/handle/ufscar/6634.

[61] L.R. Pereira, M.S.A. Alves, Dyes—environmental impact and remediation, in: A. Malik, G. Elisabeth (Eds.), Environ. Prot. Strateg. Sustain. Dev. Strateg. Sustain. Springer, Netherlands, Dordrecht, 2012, pp. 111–162, , https://doi.org/10.1007/978-94-007-1591-2_4.

[62] P. Grenni, V. Ancona, A. Barra Caracciolo, Ecological effects of antibiotics on natural ecosystems: a review, Microchem. J. 136 (2018) 25–39, https://doi.org/10.1016/j.microc.2017.02.006.

[63] K. Ji, S. Kim, S. Han, J. Seo, S. Lee, Y. Park, K. Choi, Y.L. Kho, P.G. Kim, J. Park, K. Choi, Risk assessment of chlortetracycline, oxytetracycline, sulfamethazine, sulfathiazole, and erythromycin in aquatic environment: are the current environmental concentrations safe? Ecotoxicology 21 (2012) 2031–2050, https://doi.org/10.1007/s10646-012-0956-6.

[64] K. Ji, K. Choi, S. Lee, S. Park, J.S. Khim, E.H. Jo, K. Choi, X. Zhang, J.P. Giesy, Effects of sulfathiazole, oxytetracycline and chlortetracycline on steroidogenesis in the human adrenocarcinoma (H295R) cell line and freshwater fish Oryzias latipes, J. Hazard. Mater. 182 (2010) 494–502, https://doi.org/10.1016/j.jhazmat.2010.06.059.

[65] R. Su, R. Bechstein, L. So, R.T. Vang, M. Sillassen, B. Esbjornsson, A. Palmqvist, F. Besenbacher, How the anatase-to-rutile ratio influences the photoreactivity of TiO2, J. Phys. Chem. C 115 (2011) 24287–24292.

[66] K.I. Ishibashi, A. Fujishima, T. Watanabe, K. Hashimoto, Detection of active oxidative species in TiO2 photocatalysis using the fluorescence technique, Electrochem. Commun. 2 (2000) 207–210, https://doi.org/10.1016/S1388-2481(00)00006-0.

[67] H.M. Rietveld, A profile refinement method for nuclear and magnetic structures, J. Appl. Crystallogr. 2 (1969) 65–71, https://doi.org/10.1107/S0021889869006558.

[68] P. Kubelka, F. Munk, Ein Beitrag Zur Optik Der Farbanstriche, Zeitschrift Für Tech. Phys. 12 (1931) 593–601.

[69] A.A.A. Ahmed, Z.A. Talib, M.Z. Bin Hussein, A. Zakaria, Improvement of the crystallinity and photocatalytic property of zinc oxide as calcination product of Zn-Al layered double hydroxide, J. Alloys Compd. 539 (2012) 154–160, https://doi.org/10.1016/j.jallcom.2012.05.093.

[70] G. Xi, J. Ye, Synthesis of bismuth vanadate nanoplates with exposed {001} facets and enhanced visible-light photocatalytic properties, Chem. Commun. 46 (2010) 1893, https://doi.org/10.1039/b923435g.

[71] Y. Luo, G. Tan, G. Dong, H. Ren, A. Xia, A comprehensive investigation of tetragonal Gd-doped BiVO4 with enhanced photocatalytic performance under sun-light, Appl. Surf. Sci. 364 (2016) 156–165, https://doi.org/10.1016/j.apsusc.2015.12.100.

[72] M. Blue, D. Mechanism, A. Novel, Simple and Green Way to Fabricate BiVO4 Methylene Blue Decomposition Mechanism Vol. 3 (2016), pp. 1–11, https://doi.org/10.3390/cryst6070081.

[73] J. Yi, Z. Zhao, D. Zhou, C. Ma, Y. Cao, J. Qiu, Monophasic zircon-type tetragonal Eu1-xBixVO4 solid-solution: synthesis, characterization, and optical properties, Mater. Res. Bull. 57 (2014) 306–310, https://doi.org/10.1016/j.materresbull.2014.04.068.

[74] J.K. Cooper, S. Gul, F.M. Toma, L. Chen, Y.-S.S. Liu, J. Guo, J.W. Ager, J. Yano, I.D. Sharp, Indirect bandgap and optical properties of monoclinic bismuth vanadate, J. Phys. Chem. C 119 (2015) 2969–2974, https://doi.org/10.1021/jp512169w.

[75] A. Walsh, Y. Yan, M.N. Huda, M.M. Al-Jassim, S.-H.H. Wei, Band Edge electronic structure of BiVO4: elucidating the role of the Bi s and V d orbitals, Chem. Mater. 21 (2009) 547–551, https://doi.org/10.1021/cm802894z.

[76] J. Wiktor, I. Reshetnyak, F. Ambrosio, A. Pasquarello, Comprehensive modeling of the band gap and absorption spectrum of BiVO4, Phys. Rev. Mater. 1 (2017) 022401, , https://doi.org/10.1103/PhysRevMaterials.1.022401.

[77] A. Zhang, J. Zhang, N. Cui, X. Tie, Y. An, L. Li, Effects of pH on hydrothermal synthesis and characterization of visible-light-driven BiVO4 photocatalyst, J. Mol. Catal. A Chem. 304 (2009) 28–32, https://doi.org/10.1016/j.molcata.2009.01.019.

[78] G. Wang, W. Qin, J. Zhang, L. Wang, G. Wei, P. Zhu, R. Kim, Controlled synthesis and luminescence properties from cubic to hexagonal NaYF4:Ln3 + (Ln = Eu and Yb/Tm) microcrystals, J. Alloys Compd. 475 (2009) 452–455, https://doi.org/10.1016/j.jallcom.2008.07.050.

[79] K.W. Kramer, D. Biner, G. Frei, H.U. Gudel, M.P. Hehlen, S.R. Luthi, Hexagonal sodium yttrium fluoride based green and blue emitting upconversion phosphors, Chem. Mater. 16 (2004) 1244–1251, https://doi.org/10.1021/cm031124o.

[80] G. De, W. Qin, J. Zhang, J. Zhang, Y. Wang, C. Cao, Y. Cui, Infrared-to-ultraviolet up-conversion luminescence of YF3:Yb3 +, Tm3 + microsheets, J. Lumin. 122–123 (2007) 128–130, https://doi.org/10.1016/j.jlumin.2006.01.120.

[81] D. Chen, Y. Wang, Y. Yu, P. Huang, Intense ultraviolet upconversion luminescence from Tm3 +/Yb 3 +:??-YF3 nanocrystals embedded glass ceramic, Appl. Phys. Lett. 91 (2007) 30–33, https://doi.org/10.1063/1.2767988.

[82] S. Tokunaga, H. Kato, A. Kudo, Selective preparation of monoclinic and tetragonal BiVO4 with scheelite structure and their photocatalytic properties, Chem. Mater. 13 (2001) 4624–4628, https://doi.org/10.1021/cm0103390.

[83] G. Li, Y. Bai, W.F. Zhang, Difference in valence band top of BiVO4 with different crystal structure, Mater. Chem. Phys. 136 (2012) 930–934, https://doi.org/10.1016/j.matchemphys.2012.08.023.